



THE UNIVERSITY *of* EDINBURGH

Edinburgh Research Explorer

Structural elements promote architectural stripe formation and facilitate ultra-long-range gene regulation at a human disease locus

Citation for published version:

Chen, L-F, Long, HK, Park, M, Swigut, T, Boettiger, AN & Wysocka, J 2023, 'Structural elements promote architectural stripe formation and facilitate ultra-long-range gene regulation at a human disease locus', *Molecular Cell*. <https://doi.org/10.1016/j.molcel.2023.03.009>

Digital Object Identifier (DOI):

[10.1016/j.molcel.2023.03.009](https://doi.org/10.1016/j.molcel.2023.03.009)

Link:

[Link to publication record in Edinburgh Research Explorer](#)

Document Version:

Peer reviewed version

Published In:

Molecular Cell

General rights

Copyright for the publications made accessible via the Edinburgh Research Explorer is retained by the author(s) and / or other copyright owners and it is a condition of accessing these publications that users recognise and abide by the legal requirements associated with these rights.

Take down policy

The University of Edinburgh has made every reasonable effort to ensure that Edinburgh Research Explorer content complies with UK legislation. If you believe that the public display of this file breaches copyright please contact openaccess@ed.ac.uk providing details, and we will remove access to the work immediately and investigate your claim.



1 **HOIST: Evidence-Driven Spatio-Temporal COVID-19**

2 **Hospitalization Prediction with Ising Dynamics**

3 Junyi Gao^{1,2}, Joerg Heintz³, Christina Mack⁴, Lucas Glass⁴, Adam Cross^{5*}, Jimeng Sun^{3*}

4 1 The University of Edinburgh, Edinburgh, Edinburgh, UK

5 2 Health Data Research UK, UK

6 3 University of Illinois Urbana Champaign, Champaign, IL, USA

7 4 IQVIA, Cambridge, Massachusetts, USA

8 5 University of Illinois, College of Medicine Peoria, Department of Research Services, Peoria, IL,
9 USA

10 * Correspond to Adam Cross (arcross@uic.edu) and Jimeng Sun (jimeng@illinois.edu)

11

12 **Abstract**

13 In this work, we aim to accurately predict the number of hospitalizations during the COVID-19
14 pandemic by developing a spatio-temporal prediction model. We propose HOIST, an Ising
15 dynamics-based deep learning model for spatio-temporal COVID-19 hospitalization prediction. By
16 drawing the analogy between locations and lattice sites in statistical mechanics, we use the Ising
17 dynamics to guide the model to extract and utilize spatial relationships across locations and model
18 the complex influence of granular information from real-world clinical evidence. By leveraging rich
19 linked databases, including insurance claims, census information, and hospital resource usage data
20 across the U.S., we evaluate the HOIST model on the large-scale spatio-temporal COVID-19
21 hospitalization prediction task for 2,299 counties in the U.S. In the 4-week hospitalization prediction
22 task, HOIST achieves 368.7 mean absolute error, 0.6 R^2 and 0.89 concordance correlation
23 coefficient score on average. Our detailed number needed to treat (NNT) and cost analysis suggest
24 that future COVID-19 vaccination efforts may be most impactful in rural areas. This model may
25 serve as a resource for future county and state-level vaccination efforts.

26

27 **Introduction**

28 The COVID-19 pandemic has caused the enormous social and economic loss. With over 90
29 million confirmed cases and 1 million deaths in the U.S. by Aug 2022¹, the pandemic placed a heavy
30 burden on national and global healthcare systems. The disparities in medical resource availability
31 among U.S. counties – including ventilators, hospital beds, and critical care staff – can and, in some
32 cases, have devastatingly impacted patient outcomes². Nationwide vaccination efforts have
33 primarily favored urban areas, and the urban-rural disparity in vaccination coverage has continued
34 to worsen throughout the pandemic³. Rural vaccination efforts are technically challenging due to a
35 combination of more limited access to healthcare, generally lower perception of the severity of
36 COVID-19 by residents of rural communities, and usually higher levels of vaccine hesitancy³. This
37 multi-year trend of relative rural under-immunization raises the question of whether further
38 vaccination efforts might be more impactful in these under-immunized areas regarding
39 hospitalization, death, and cost-effectiveness. Answering this question is technically challenging but
40 clinically meaningful; if counties can be stratified in terms of improved outcomes per vaccination,

41 this may provide meaningful insight into how local and statewide efforts might be distributed to
42 maximize impact. To accomplish this task, we propose the following technical contributions:

- 43 1. Extracting inter-region similarities. The pandemic progression might be similar in regions with
44 similar geographical and socioeconomic properties. If so, extracting and utilizing these
45 similarities would help the model better predict pandemic progression in the future. Most
46 existing spatio-temporal pandemic prediction methods use pre-defined location graphs to
47 explicitly inform the spatial connections to the model⁴⁻⁷. In contrast, these manually defined
48 location graphs may differ significantly from the ground truth inter-regional relationships. Other
49 works learn the spatial connectivity purely based on the historical pandemic progressions^{8,9},
50 regardless of the underlying social, economic, or geographical similarities, which cannot
51 capture the inter-region similarities in full view and lead to inferior prediction results. Therefore,
52 it is non-trivial to model spatial dependencies with multi-source background data in a flexible
53 way.
- 54 2. Utilizing complex inner-region influence factors. Local COVID-19 hospitalization rates are
55 likely affected by many factors, including the number of infected patients, high-risk patient
56 population size, and vaccination rates. Estimating these effects becomes more challenging with
57 more granular information, such as the number of COVID-19 immunizations per individual.
58 Leveraging these complex inner-region influence factors, such as medical claims and
59 vaccination statistics, may significantly improve hospitalization prediction performance.
60 Recent research combines the susceptible-infected-removed (SIR) and susceptible-exposed-
61 infected-removed (SEIR) differential models with deep learning models to improve predictions
62 by simulating real-world SIR dynamics⁴⁻⁷. However, when applied to hospitalization prediction
63 tasks, these models face the following issues: (1) Limited data sources and model parameters
64 in the traditional epidemiological model make it difficult to utilize these complex high-
65 dimensional inner-region factors effectively. Ignoring complex inner-region factors may cause
66 the model to fail to capture the underlying disease distribution, virus subvariants, and
67 vaccination effectiveness rates across the state, which could lead to biased results. While purely
68 deep-learning-based time series prediction models such as recurrent neural networks (RNN)
69 can handle high-dimensional data and extract complex nonlinear relationships, they ignore real-
70 world progression dynamics and have minimal interpretability compared to epidemiological
71 based models. (2) Most epidemiological models offer a simple increasing-decreasing trend with
72 different rates, while the hospitalization curves are more complex and may not follow this
73 simple trend. (3). Moreover, the SIR dynamics are not designed for spatio-temporal prediction
74 tasks, so these models cannot directly utilize for hospitalization prediction.

75 To address the above challenges, we propose an Ising dynamics-based deep learning model for
76 spatio-temporal COVID-19 hospitalization prediction. We have combined multiple data sources,
77 including disease and vaccination statistics from real-world medical claims, medical resource usage,
78 census, and geographical and mobility data, to create an evidence hub for the ability to train a
79 complex evidence-driven spatio-temporal prediction model, HOIST. The proposed HOIST model
80 can handle complex inner-regional influence factors from multiple data sources and adaptively learn
81 the inter-regional relationships using the locational census and geographical and inter-locational
82 mobility data without requiring a pre-defined location graph with fixed edges.

83 The model learning process is guided by the Ising dynamics, a mathematical statistical
84 mechanics model to estimate site spin configurations in square lattices¹⁰. By drawing the analogy

85 between locations and lattice sites, we find the Ising dynamics a natural choice to model the inner-
86 region factors and inter-region similarities simultaneously: (1) the Ising dynamics guide the model
87 to extract and utilize inter-region spatial relationships by taking prediction results from similar
88 locations as kinetic energy; (2) the Ising dynamics model the complex influence of granular inner-
89 region factors from the real-world clinical evidence as potential energy (i.e., external fields). Both
90 kinetic energy and potential energy jointly decided the energy of the location (predicted
91 hospitalization case to increase or decrease). The Ising dynamics in this paper are used as a
92 regularizer to guide the model learning and prediction process, which enables the model to learn
93 complex nonlinear patterns flexibly. We use recurrent neural networks (RNN) to learn the
94 parameters of the Ising model so our model can also extract and utilize temporal patterns in the data.

95 The overview of HOIST is shown in **Figure 1**. The HOIST model first uses static data to
96 calculate the distances between locations in the latent space. These distances are further normalized
97 into 0 and 1, which indicate the connectivity between locations learned by the model. The dynamic
98 data are used to estimate the External Fields (E.F.s) of locations and used to generate predictions
99 with LSTM. The estimated E.F.s and the learned connectivity are used to calculate the Ising dynamic
100 loss, which is then used to regularize the prediction results and better model the real-world
101 connectivity and effects of various influence factors.

102 We evaluate the HOIST model on the large-scale spatio-temporal COVID-19 hospitalization
103 prediction task for 2,299 counties in the United States. This scale is much larger and more granular
104 than existing COVID-19 spatio-temporal predictive works. In the 4-week hospitalization prediction
105 task, HOIST achieves 368.7 MAE, 0.6 R^2 and 0.89 CCC scores. We also conduct experiments with
106 different lengths of prediction windows from 1 week to 5 weeks. Compared to the best baseline
107 model, HOIST achieves 48% lower MAE, 65% lower MSE, 272% higher R^2 and 51% higher CCC
108 on average. The prediction performances under the temporal data split setting show that HOIST can
109 consistently achieve low prediction error regardless of the underlying data distribution shift caused
110 by new virus variants. These results suggest the HOIST model can accurately predict both long-
111 term trends and short-term variations, enabling broader real-world applications.

112 Unlike totally black-box deep learning time-series models, the fusion of real-world dynamics
113 in HOIST allows us to look deeper into the model to see how various influence factors affect the
114 model predictions. By analyzing the weights of external fields, we find that the booster vaccination
115 rate has a more significant negative correlation with future hospitalization cases (i.e., more profound
116 impact) compared to the first and second vaccinations in the series. We also find that the effects of
117 two major vaccination brands, Pfizer and Moderna, have no statistical difference in our model. By
118 simulating varying immunization rates, we conduct a detailed analysis of the marginal benefit of the
119 vaccination ratio by answering two questions: (1) How many more vaccinations are necessary to
120 prevent one hospitalization case for a specific location? (2) What is the cost ratio between these
121 vaccinations and the average COVID-19 hospitalization for a specific location? Quantitatively, our
122 model shows that increasing the vaccination ratio by 10% can reduce the number of current
123 hospitalization cases by 15% on average for all locations. We also find that the cost ratio is generally
124 highest in much of the rural Midwest and Rock Mountain regions, suggesting that prioritization of
125 vaccine efforts in these counties could most significantly reduce the overall statewide healthcare
126 financial burden of COVID-19. For 368 counties among 43 states all over the United States, rural
127 vaccination outreach efforts are likely cost-saving endeavors. We believe these results and our
128 model may inform clinicians, healthcare institutions, and policymakers to improve their decisions

129 and ultimately reduce the negative economic and health impacts caused by the pandemic. All
130 detailed county-level analysis results are available at the online visualization platform at
131 <https://v1xerunt.github.io/HOIST/>.

132 Results

133 Problem formulation and data sources

134 We develop the HOIST model to predict the total number of COVID-19 hospitalization cases
135 in an upcoming four-week period at a county level across the United States. Throughout this paper,
136 we use N to denote the number of locations (counties) and T to denote the length of timesteps
137 (days). The model uses static location background data to adaptively learn location connectivity and
138 then uses dynamic data to learn the temporal patterns. The model uses the learned spatio-temporal
139 patterns to conduct predictions. Concretely, we formulate model inputs and the prediction task as
140 follows:

141 **Input 1 (Static Data).** The static data include the distance matrices $\mathbf{D}, \mathbf{G} \in \mathbb{R}^{N \times N}$, population
142 demographics statistics $\mathbf{M} \in \mathbb{R}^{N \times 9}$ and economics and healthcare statistics $\mathbf{E} \in \mathbb{R}^{N \times 4}$. \mathbf{D} is the
143 geographical distance matrix and \mathbf{G} is the mobility distance matrix. The geographical distances are
144 the Haversine distances between N locations. The mobility distance includes the average mobility
145 flows between N locations during 2020 and 2021. The mobility scores are collected from the
146 Multiscale Dynamic Human Mobility Flow Dataset, which analyzed millions of anonymous mobile
147 phone users' visits to various places provided by SafeGraph¹¹. The census features \mathbf{M}, \mathbf{E} include
148 populations of different age and race groups and medical resource statistics, which are collected
149 from the county-level census dataset provided by¹².

150 **Input 2 (Dynamic Data).** All dynamic data are three-dimensional tensors, including the daily new
151 infected COVID-19 case counts $\mathbf{I} \in \mathbb{R}^{N \times T \times 1}$, medical claim statistics $\mathbf{C} \in \mathbb{R}^{N \times T \times 20}$, vaccination
152 statistics $\mathbf{V} \in \mathbb{R}^{N \times T \times 17}$, and medical resource usage statistics $\mathbf{U} \in \mathbb{R}^{N \times T \times 4}$. The daily new cases \mathbf{I}
153 are collected from the Johns Hopkins COVID-19 Data Repository¹³. Claim statistics \mathbf{C} include
154 daily statistics of total patients, patients older than 65, and patients with certain comorbidities. The
155 age threshold and comorbidities are derived from the CDC COVID-19 guidelines¹⁴ and the Charlson
156 Comorbidity Index¹⁵. The vaccination statistics \mathbf{V} include daily statistics of 13 different
157 vaccination CPT codes. Both vaccination and claim statistics are collected from IQVIA's real-world
158 claims dataset¹⁶. The medical resource usage statistics \mathbf{U} include the usage of inpatient and ICU
159 beds and their usage for COVID-19 patients, which are collected from HealthData.gov¹⁷. Though
160 \mathbf{U} also provide the information for hospitalization cases, we use \mathbf{C} instead of \mathbf{U} as the ground-
161 truth case numbers. This is because \mathbf{U} only provides weekly statistics and the statistics are collected
162 from fewer healthcare institutions compared to the claims data. We include medical resource usage
163 statistics \mathbf{U} to help reduce the potential biases in the claims data.

164 The feature list and statistics can be found in the Supplementary Information.

165 **Task (Spatio-temporal COVID-19 Hospitalization Prediction).** Given all static and dynamic data
166 of N locations and T timesteps, our task is to predict the total number of COVID-19
167 hospitalization cases in future L days for each of the N locations, denoted as $\mathbf{y} \in \mathbb{R}^N$. Since the
168 claims data do not show the primary cause for hospitalizations, we define a hospitalization case as
169 a patient hospitalized within 35 days after the COVID-19 diagnosis in the claims dataset and we
170 calculate the total hospitalization cases for each location to get \mathbf{y} . This setting is inspired by

171 previous COVID-19 hospitalization prediction works^{18,19}.

172 Experiment settings

173 In the experimental phase, we extract all the required data from September 2020 to May 2022.
174 We set the input window τ to 5 weeks and the prediction window L to 4 weeks. We select counties
175 using the FIPS codes. The final number of counties are 2,299. We only exclude counties that have
176 zero cases for all timesteps. Note that our experiment scale is much larger and more granular than
177 existing works^{4,5}, which allows for a wider scope of possible applications.

178 We use the mean square error (MSE), mean absolute error (MAE), the coefficient of
179 determination (R^2), and the average concordance correlation coefficient (CCC) to evaluate model
180 prediction. The CCC and R^2 are computed as:

$$181 \quad R^2 = 1 - \frac{\sum(\hat{y}_i - y_i)^2}{\sum(\hat{y}_i - \mu_y)^2} \quad (1)$$

$$182 \quad \text{CCC} = \frac{2\rho\sigma_{\hat{y}}\sigma_y}{\sigma_{\hat{y}}^2 + \sigma_y^2 + (\mu_{\hat{y}} - \mu_y)^2} \quad (2)$$

183 where $\mu_{\hat{y}}$ and μ_y are the means for the predictions and ground-truth, and $\sigma_{\hat{y}}^2$ and σ_y^2 are the
184 corresponding variances. ρ is the correlation coefficient between the two variables \hat{y} and y . Note
185 that the range of R^2 is $(-\infty, 1)$, so an extreme value may significantly affect the average value. In
186 contrast, the range of CCC is $(-1, 1)$, so this will be less affected by extreme values.

187 We split the sequence into train, validation, and test sets in a 3:1:1 ratio. The training sequences
188 are from Sep 04, 2020 to Sep 02, 2021; the validation sequences are from Sep 03, 2021 to Dec 23,
189 2021, and the test sequences are from Dec 24, 2021 to Apr 15, 2022. We train the model on the
190 training set and save the model and hyper-parameters with the best performance on the validation
191 set. We then test the model on the testing set and report the performance. We train all models 5 times
192 with different random initializations and calculate the standard deviations. Due to diverse location
193 characteristics, the average hospitalization cases vary from a few to tens of thousands of cases. This
194 large variation in case numbers poses a challenge for the deep learning model to learn stable
195 parameters. We therefore conduct the log transformation on the prediction targets and scale the
196 model predictions back to the original scale, then calculate the performance metrics. We also provide
197 the prediction uncertainty at 90% confidence in all county-level and state-level prediction plots
198 using the conformal methods²⁰. The conformal algorithms possess explicit and non-asymptotic
199 guarantees without distributional assumptions or model assumptions, so that they can be easily
200 applied to all trained models. The prediction interval α is estimated as:

$$201 \quad \alpha = [\hat{y} - s\sigma, \hat{y} + s\sigma] \quad (3)$$

202 where \hat{y} is the average prediction using the 5 models with different random initializations, σ
203 denotes the standard deviation of 5 models. The value of parameter s depends on the required
204 confidence. For example, if we aim to obtain the prediction interval with 90% confidence, we use
205 calculate the s to make the prediction interval α covers 90% ground truth on the validation set.
206 Then we applied the s on the test set to calculate the test prediction interval. We provide more
207 detailed model uncertainty analysis in the Supplementary Information.

208 We use Python 3.9, PyTorch 1.12²¹, scikit-learn 1.2, NumPy 1.19 to collect the data and
209 implement the models. We use the mini-batch gradient descent strategy to train the models and the
210 batch size is set to 128. We use Adam optimizer with learning rate 0.01 for 300 epochs. We save the

211 model with the highest score on the validation set and report the prediction performances on the
212 testing set. All the experiments are done on the server with Intel i9-13900K CPU, 64 GB RAM and
213 one NVIDIA RTX 4090 GPU. The HOIST source code is publicly available on GitHub
214 (<https://github.com/v1xerunt/HOIST>).

215 **Baseline models**

216 We compare HOIST with the following epidemiology and deep-learning methods.

- 217 1. **DELPHI-SEIR**²²: This is a variant of the SEIR (susceptible, exposed, infectious, and
218 recovered) epidemiology model. Compared with the traditional SEIR model, DELPHI-
219 SEIR can model hospitalization trends and policy strategies. We use the trust region²³
220 optimization strategy to estimate the model's parameters.
- 221 2. **GRU**: We input all features into a gated recurrent unit (GRU) model and predict the future
222 number of cases. The GRU model is a variant of RNN, widely applied in multiple pandemic
223 prediction works²⁴⁻²⁶. The hidden dimension of GRU is set to 128.
- 224 3. **LSTM**: We input all features into a long short-term memory (LSTM) model and predict
225 the future number of cases. The LSTM model is another variant of RNN. The hidden
226 dimension of LSTM is also set to 128.
- 227 4. **ColaGNN**⁹: ColaGNN learns the location graph with sequential data to learn spatial
228 relationships for pandemic progression. The hidden dimension of RNN is set to 128, and
229 the convolution filter dimension is set to 64.
- 230 5. **ACTS**⁸: ACTS is a COVID-19 forecasting model which uses the inter-series attention
231 mechanism to learn spatial relationships between locations. The convolution filter
232 dimension is set to 64 and the segment length is set to 14.
- 233 6. **CovidGNN**²⁷: CovidGNN uses a graph neural network with skip connections to predict
234 future COVID-19 cases. We use a two-layer graph attention network, and the graph network
235 dimension is set to 64.
- 236 7. **STAN**⁴: STAN fuses the SIR dynamics into a spatio-temporal prediction model for
237 COVID-19 case prediction. The graph network dimension is set to 64, and the hidden
238 dimension of GRU is set to 128. Since the SIR dynamics do not apply to the hospitalization
239 prediction task, we remove the SIR constraints in the STAN model.

240 All models can access the same data sequences with the same input window and are all
241 evaluated on the same testing set. For the spatial-temporal prediction models (i.e., ColaGNN, ACTS,
242 CovidGNN, STAN), we use the static data to build the location graph or calculate the location
243 similarities in their algorithms. For the GRU and LSTM model, we concatenate the static data with
244 the original inputs at each timestep to the model. The SEIR model cannot take the static location
245 data as inputs. All model hyper-parameters are decided by using grid search on the validation dataset.
246 For the DELPHI-SEIR model, we use the deployed version of the DELPHI-SEIR model (i.e.,
247 DELPHI-SEIR V4) and recommended optimal parameters. To assess the performance improvement
248 from the Ising dynamics, the adaptative connectivity learning, and the real-world evidence, we
249 conduct an ablation study by comparing HOIST against the following ablation versions from both
250 a data perspective and a method perspective:

- 251 1. **HOIST-Vaccination**: We remove the vaccination statistics data from the model input
252 sequences of HOIST.
- 253 2. **HOIST-Risk**: We remove the high-risk patient statistics in the real-world claims data from

- 254 model input sequences of HOIST.
- 255 3. **HOIST-AC**: We remove the adaptative connection learning module from HOIST. The \mathbf{S}
- 256 matrix is learned by calculating the sequence similarities instead of using location
- 257 background data.
- 258 4. **HOIST-Ising**: We remove the Ising dynamic loss and replace the E.F. modeling module
- 259 with a naïve LSTM network in HOIST.

260 **Model performance analysis**

261 We design experiments to answer the following research questions:

- 262 1. How well does HOIST perform in the hospitalization prediction task?
- 263 2. How well does HOIST perform with different lengths of prediction window?
- 264 3. How well does HOIST perform under temporal data split setting?
- 265 4. What is the analysis of the learned external field weights?
- 266 5. How does the HOIST model help to increase vaccination rates effectively?

267 **28-day hospitalization prediction performance**

268 **Table 1** shows the performance of the 28-day hospitalization prediction task. Compared to the

269 best baseline model, HOIST reaches 70% lower MSE and 50% lower MAE. It also achieves an R^2

270 score of 0.6 and a CCC of 0.89 while the best baseline model achieves 0.16 R^2 and 0.6 CCC. We

271 find ColaGNN and ACTS achieve better prediction performance among the compared models; this

272 may be because both CovidGNN and STAN require a fixed location graph structure as input, while

273 ColaGNN and ACTS can learn the spatial relationships based on the sequence similarity. Compared

274 to the infected case prediction task, the spatial patterns of hospitalization cases may be more

275 complex and thus cannot be pre-defined using a fixed location graph. Therefore, models that can

276 learn flexible connections commonly outperform all others in this task. By utilizing the location-

277 static background data, HOIST can better extract spatial patterns of the pandemic progression. We

278 also find that traditional epidemiology SEIR models fail to predict accurately in this task, probably

279 because the hospitalization curves do not follow a simple increasing-decreasing trend, which is the

280 underlying assumption of most epidemiological models. Additionally, the ground-truth curves may

281 have multiple peaks and complex short-term variations, which increases the difficulty of the

282 predictive task. Note that when calculating R^2 and CCC scores, the average value μ_y used in the

283 denominator is the average value in the test time phase, which is often difficult to beat since the

284 future μ_y is unavailable at the prediction time. Therefore, in all experiments, any positive R^2 or

285 high CCC scores can be impressive to achieve.

286 We conduct the student t -test to evaluate the significance of the performance differences. The

287 results show that the performance differences between HOIST and the best baseline models are

288 significant ($p < 0.001$). HOIST also outperforms all ablation versions of HOIST by a large margin,

289 validating the effectiveness and necessity of all proposed modules. According to the performance

290 analysis, the Ising dynamics are the most critical component of HOIST. By modeling various

291 influence factors as external fields and using spatial-temporal dynamics to regularize the model

292 learning process, HOIST confirms that the Ising dynamics can improve spatio-temporal predictive

293 performance by more closely resembling the real-world curve. Furthermore, integrating real-world

294 evidence data, such as high-risk patient cohorts and vaccination statistics can reduce prediction error.

295 Using background data to learn adaptative spatial connectivity in HOIST also enables it to

296 outperform the reduced model, which only uses sequence similarities (i.e., HOIST-AC). The
297 adaptative connectivity learning module also helps the HOIST learn clustered spatial embeddings
298 using the demographics data. We provide visualization plots of the learned embeddings in the
299 supplementary material. The results show that HOIST can not only extract geographical similarities
300 between locations, but also can identify geographically distant but socio-economically similar
301 locations. We also provide the predicted curve plots for all US states in the Supplementary
302 Information.

303 Prediction performance with different lengths of prediction window

304 In this section, we evaluate each model's long-term and short-term prediction performance by
305 changing the prediction window L from 1 week to 5 weeks and then train and evaluate all the
306 models with the same strategy. The MAE, MSE, R^2 , and CCC of HOIST and the 6 best baseline
307 models are shown in **Figure 2**. Due to its poor performance, we exclude the SEIR model.

308 The results demonstrate that the MSE and MAE of all models increase as the length of the
309 prediction window increases. This is expected since predicting further into the future becomes
310 progressively more challenging. However, HOIST consistently achieves a much lower MAE and
311 MSE than all baseline models. HOIST also achieves consistently high R^2 and CCC scores.
312 Compared to the baseline models, HOIST achieves on average a 48% lower MAE, 65% lower MSE,
313 272% higher R^2 , and 51% higher CCC. The results demonstrate that the HOIST model accurately
314 predicts both long-term trends and short-term variations, enabling broader real-world applications.

315 Prediction performance under temporal data split setting

316 New variants of COVID-19 virus can lead to different disease severity. It is non-trivial for a model to
317 accurately predict future hospitalization under such distribution transitions. We design experiments to
318 evaluate how model performance evolves over time. We use a sliding window training setting by using
319 10 weeks data for training and using next 4 weeks data for testing. We split the time from Sep 2020 to
320 April 2022 into 7 periods and the model are tested in 7 testing time phases. We compare HOIST against
321 other 3 best baseline models (i.e., LSTM, ACTS and ColaGNN). The results are shown in

322 **Figure 3.**

323 The results show that HOIST consistently outperform all baseline models in terms of MSE and
324 MAE on all testing phases. HOIST consistently achieves low prediction errors and high CCC scores
325 and is less affected by the temporal data distribution shifts. We notice that some baseline models
326 experience low prediction performance on Feb 2021 and Jan 2022. This may be due to distribution
327 shifts between training and testing data caused by emerging of new variants of the COVID-19 virus.
328 However, HOIST achieves lower prediction error than baselines on these time phases.

329 Analysis of learned external fields

330 Compared with the baseline black-box models, modeling external fields with Ising dynamics
331 allows us to analyze the importance of different factors for different locations, providing us with
332 more insight into which features are most predictive of hospitalization. In the learned E.F.
333 parameters $\hat{\mathbf{f}}$, each dimension denotes the weight of the corresponding input factor. To visualize the
334 effect of the number of vaccinations on the hospitalization rate, we plot the corresponding weights
335 of the following vaccination features: 1) total number of vaccinations, 2) number of first vaccination
336 administrations, 3) number of second vaccination administrations, and 3) number of booster

337 administrations, as shown in **Figure 4**.

338 The negative EF weights occur because vaccination ratio is negatively correlated with
339 hospitalization case count. However, the results show that the E.F. weights of all four features are
340 increasing, meaning the predictiveness of vaccinations are decreasing over time. This is possibly
341 due to the increased prevalence of new variants of the virus, many of which are more resistant to
342 vaccinations, which is consistent with conclusions in recent medical research^{28,29}. However, we can
343 still observe that the booster doses (the purple line) are more effective than the first and second
344 doses (p-value < 0.05). We also compare the model effect (i.e., the E.F. weights) of Pfizer (CPT
345 code 0001A~0004A) and Moderna (CPT code 0011A~0013A, 0064A) COVID-19 vaccines, and
346 we find that their effects do not have statistical difference in our model (p-value 0.1).

347 We also explore the E.F. weights of high-risk conditions, which are condition codes defined by
348 the CDC COVID-19 People with Certain Medical Conditions guideline¹⁴ and the Charlson
349 Comorbidity Index¹⁵. These features are proved to have significant impacts on COVID-19 patients'
350 outcomes^{30,31}. We find the feature with the highest E.F. weight is the number of patients older than
351 65. The top 5 conditions are: renal disease, dementia, immunodeficiency, malignancy, and chronic
352 lung disease. The results are consistent with CDC guidelines, and we do not observe statistically
353 significant differences in these five features.

354 Predicted hospitalization hotspot map and error analysis

355 We present the predicted hospitalization hotspot map in **Figure 5**. **Figure 5-(a)** is the hotspot
356 map colored by the number of hospitalization cases and **Figure 5-(b)** is colored by the ratio of
357 hospitalization cases over total population. There are some blank areas in the map in cases of no
358 valid data or zero case counts in these counties. These heatmaps can be accessed in an online
359 visualization platform at <https://v1xerunt.github.io/HOIST/>.

360 We find that the spatial patterns of hospitalization are similar in both figures. West coast,
361 Northeast coast and Midwest areas generally have high hospitalization case counts and per-person
362 occurrence. Interestingly, we also find that some locations – such as the San Diego county (A) and
363 Riverside county (B) along the West coast – have very high case counts but only medium-level
364 hospitalization ratios. A possible interpretation could be that the people from these counties tend to
365 travel to Los Angeles for hospitalization.

366 We also plot a heatmap to show the spatial patterns of the mean average percentage error
367 (MAPE). We only calculate the MAPE for locations where case counts are larger than 100 in the
368 testing phase because a small prediction error can lead to very large MAPE for locations with low
369 counts. The results are shown in **Figure 5-(c)**.

370 We find that HOIST achieves low MAPE for most locations, with only 15 locations having a
371 MAPE greater than 0.5. For these locations, HOIST tends to underestimate the case counts. This
372 may be because there are some pattern changes in the testing time window; for example, in
373 Effingham, Georgia, HOIST has 0.64 MAPE. When we plot the predicted hospitalization curve and
374 the number of infected cases (**Figure 6**), we find several peaks in the infected case count curve
375 during both the validation and testing phases, which is quite different from training patterns. These
376 sudden fluctuations in input features may cause HOIST to fail to accurately predict the surge of
377 hospitalization cases during the testing phase. We provide another two case examples for error
378 analysis in the Supplementary Information.

379 Number needed to treat prediction with HOIST

380 Increasing a community's vaccination rate is an effective method of reducing both the
 381 occurrence and severity of COVID-19³². However, there is still uncertainty surrounding how and
 382 whether this effectiveness is influenced by local vaccination rates. In other words, we ask the
 383 question, "Due to the disproportionately higher vaccination rates in urban areas, do inequalities exist
 384 regarding the number of additional vaccinations necessary to reduce a single hospitalization or
 385 death?" We also calculate the cost effectiveness of future vaccination efforts based on the county-
 386 level average cost of COVID-19 hospitalization. Accurately answering these questions at the county
 387 level may allow policymakers and healthcare institutions with limited distribution capabilities and
 388 finite medical resources to develop more targeted vaccination efforts.

389 The high predictive accuracy of HOIST enables us to answer these questions. By changing the
 390 vaccination rates in the input features, HOIST can simulate the changes of the predicted
 391 hospitalization curve. We use the predicted number of hospitalizations to calculate the Number
 392 Needed to Treat (NNT) with respect to how many vaccinations are needed to prevent one
 393 hospitalization at each county. For each location, we increase the vaccination rate by 10% (i.e., 10%
 394 total population) and calculate the predicted hospitalization case reduction between the original
 395 prediction \hat{y} and the simulated prediction \hat{y}_{sim} . The NNT for hospitalization is calculated as:

$$396 \quad NNT_h = \frac{1}{CER - EER} = \frac{1}{\left(\frac{\hat{y}}{0.1p} - \frac{\hat{y}_{sim}}{0.1p}\right)} = \frac{p}{10(\hat{y} - \hat{y}_{sim})} \quad (4)$$

397 where CER denotes the control event rate (original predicted hospitalization rate), EER denotes
 398 the experimental event rate (simulated hospitalization rate after the vaccination rate increases by
 399 10%), and p denotes the population size of the location.

400 Furthermore, we acknowledge that morbidity and mortality among individuals hospitalized
 401 with COVID-19 occur disproportionately in certain ethnic and racial minority groups. To address
 402 these outcome disparities in our model, we adjust the NNT for each county based on its
 403 demographics and their respective risk ratios:

$$404 \quad NNT_a = \frac{NNT_h}{1 * r_{white,nh} + 0.8 * r_{asian,nh} + 1.7 * r_{black,nh} + 1.8 * r_{hispanic}} \quad (5)$$

405 where $r_{white,nh}$, $r_{asian,nh}$ and $r_{black,nh}$ denote the population ratio of White, Asian, and Black
 406 non-Hispanic persons, and $r_{hispanic}$ denotes the population ratio of Hispanic or Latino persons. All
 407 county-level population ratios are extracted from the census data. The risk adjustment factor for
 408 each race and ethnicity is based on national COVID-19 death risk ratios reported by the CDC^{33,34}.
 409 While NNT_h represents the predicted number of vaccinations needed to prevent one hospitalization,
 410 NNT_a is not a direction calculation of NNT for death prevention; instead, its purpose is to illustrate
 411 how locations with similar NNT_h might be further stratified based on the predicted outcomes of
 412 those predicted hospitalizations. The resultant NNT_a favors locations with more Black/African
 413 American, Hispanic, and Latino populations. Future analytical and predictive efforts incorporating
 414 county-level death rates are warranted.

415 The heatmaps of NNT_h and NNT_a are shown in **Figure 7**. Note how the count and ratio maps
 416 identify hotspots primarily among urban and metropolitan areas. In contrast, the NNT values are
 417 generally lowest in the rural region, which are highly clustered in certain states, including North
 418 Dakota, South Dakota, Kansas, Nebraska, Montana, etc. Quantitatively, increasing the vaccination

419 ratio by 10% can reduce the number of current hospitalization cases by 15% on average for all
420 locations.

421 We further calculate the cost ratio between state average vaccination costs and state average
422 COVID-19 hospitalization costs. We collect the state-level average vaccine cost from the Centers
423 for Medicare and Medicaid Services (CMS)³⁵ and hospitalization cost for both complex and
424 noncomplex COVID-19 inpatients from the COVID-19 Cost Tracker³⁶. The cost ratio is then
425 calculated as:

$$426 \quad r_{\text{cost}} = \frac{r_{\text{complex}} * c_{\text{complex}} + r_{\text{noncomplex}} * c_{\text{noncomplex}}}{\text{NNT}_h * c_{\text{shot}}} \quad (6)$$

427 where r_{complex} and $r_{\text{noncomplex}}$ are the average complex and noncomplex COVID-19 inpatients
428 ratio extracted from the hospital resource data. c_{complex} and $c_{\text{noncomplex}}$ are hospitalization costs
429 for complex and noncomplex COVID-19 inpatients. c_{shot} is the cost of one vaccine. All
430 parameters to calculate the r_{cost} vary by location.

431 The cost ratio heatmap is shown in **Figure 7-(c)**. A cost ratio greater than 1 indicates that
432 increasing the number of vaccinations in that location by the NNT is less expensive than the cost of
433 the single prevented hospitalization. The heatmap demonstrates a ratio favoring future vaccination
434 efforts in primarily rural regions, most commonly among centrally located and landlocked counties.
435 We list the NNT_h and NNT_a of the top 15 locations with the highest (most favorable) cost ratios
436 in **Table 2**. The full county-level table can be accessed in the GitHub repository and the visualization
437 platform. These results suggest three meaningful conclusions. First, even small-scale vaccination
438 efforts in targeted counties are likely to prevent at least one hospitalization and its related sequelae.
439 Secondly, rural vaccination outreach efforts are likely cost-saving endeavors in 368 counties among
440 43 states (with cost ratio > 1). Thirdly, we find that locations that have high cost ratio also have high
441 adjust ratio. This may indicate large healthcare disparities for different race in these locations. More
442 life could be saved by improving the vaccination fairness in these locations.

443 Discussion

444 In this work, we propose an Ising dynamics-based deep learning model, HOIST, for spatio-
445 temporal COVID-19 hospitalization prediction. The HOIST model is built with multiple data
446 sources including disease and vaccination statistics from real-world medical claims, medical
447 resource usage, census, geographical and mobility data. HOIST can handle complex inner-region
448 influence factors and adaptively learn the inter-regional relationships without requiring a pre-
449 defined location graph with fixed edges. By drawing the analogy between locations and lattice sites,
450 we use the Ising dynamics as a regularizer to guide the model learning and prediction process, which
451 is a natural choice to model the inner-region factors and inter-region similarities simultaneously.

452 We evaluate the HOIST model on the large-scale spatio-temporal COVID-19 hospitalization
453 prediction task for 2,299 counties in the United States. In the 4-week hospitalization prediction task,
454 HOIST achieves 368.7 MAE, 0.6 R^2 and 0.89 CCC scores. For different lengths of prediction
455 window from 1 week to 5 weeks, HOIST achieves 48% lower MAE, 65% lower MSE, 272% higher
456 R^2 and 51% higher CCC on average compared to the best baseline models. We conducted a detailed
457 analysis of the model results and learned parameters. We find that the booster shot of vaccination
458 population percentage has a more significant negative correlation to future hospitalization cases
459 than the first and second vaccination shots. We also find that the effects of two major vaccination
460 brands, Pfizer and Moderna, have no statistical difference in our model.

461 We note that, in contrast to many previous models, our HOIST-based clinical and economic
462 predictions suggest a need to prioritize future vaccination efforts in rural areas over urban centers.
463 The results indicate that increasing the total vaccination ratio by 10% can make the number of
464 current hospitalization cases reduce by 15% on average for all locations. We believe these
465 predictions accurately reflect the growing disparity in vaccination rates between these communities.
466 Additionally, we note a positive correlation between vaccination rate and NNT; in fact, the adjusted
467 NNT map appears strikingly similar to maps depicting percentages of fully vaccinated residents by
468 county³⁷. We surmise that communities with lower-than-average proportions of vaccinated
469 individuals are more likely to benefit from further vaccination efforts irrespective of rurality. For
470 368 counties among 43 states, increasing vaccination ratio in these counties can significantly reduce
471 the overall healthcare costs for COVID-19 patients. We hope these results and our model can inform
472 clinicians, healthcare institutions, and policymakers to improve their decisions and ultimately
473 reduce the negative economic and health impacts caused by the pandemic.

474 This research is not without limitations. In the data collection process, the number of
475 hospitalization cases may have bias. We define a hospitalization case as a patient hospitalized within
476 35 days after the COVID-19 diagnosis. We extract these statistics from the claim dataset, so we
477 cannot know if COVID-19 is the primary cause of hospitalization. Though this definition is the
478 same with existing COVID-19 prediction works^{38,39}, the model may conflate hospitalizations trends
479 due to other causes with those accurately attributed to COVID-19. This is especially true in the
480 pediatric population where COVID-19 infectivity is high but severe cases are uncommon. Despite
481 these limitations, we still select claims data as our primary data source as it provides valuable
482 granular county-level statistics.

483 The second limitation concerns data preprocessing. The original data distribution of
484 hospitalization cases is highly skewed. Our dataset is much larger than previous research; over 80%
485 of locations have fewer than 1,000 hospitalization cases in the 28-day prediction window, and only
486 2% have more than 10,000 hospitalization cases. To maintain the stability of the machine learning
487 models, we conduct a log transformation on the prediction target, followed by a z-score
488 transformation to normalize the sequence. Therefore, model prediction results require two reverse
489 transformations to return to the original scale. This transformation may cause a small error in the
490 prediction scale to grow exponentially as it converts to the original scale. As a result, we observe
491 that baseline models sometimes have abnormal large prediction errors and standard deviations (e.g.,
492 over 10,000 MAE), especially when the prediction window is long. We manually remove these
493 outliers from the performance table. Though we do not find these issues in HOIST, which further
494 demonstrates the stability of the model, we still believe this is an open research challenge in the
495 large-scale spatio-temporal prediction work. The data scale issue might be solved by proposing more
496 advanced preprocessing techniques or new scale-invariant models.

497 A third limitation exists at the methodology level. Though the spatial connectivity learning
498 module is more flexible than previous works requiring fixed graph structures, the learned
499 connectivity does not change with time. In real-world scenarios, spatial connectivity may be affected
500 by several factors, including weather, holidays, and travel restrictions. Therefore, future works may
501 include integrating more data sources such as real-time mobility data between locations to further
502 improve the extracted spatial patterns, interpretability analysis on the feature contributions and more
503 granular age information. Besides, the Ising dynamics maybe not the only choice to model the
504 spatial and social background factors for hospitalization prediction. The reason we choose the Ising

505 dynamics is that it can incorporate both inter-region spatial relationships and inner-region factors
506 and can handle these complex factors compared to naïve SIR and SEIR models. We are inspired by
507 previous sociology studies that use Ising models for human behavior tendencies⁴⁰. Though the Ising
508 dynamics show good prediction performances in HOIST, we hope our exploratory work can provide
509 more inspiration for future studies using other real-world dynamics.

510 **Methods**

511 We follow the recommendations set out in the Global Code of Conduct for Research in
512 Resource-Poor Settings when designing, executing and reporting the research and this research does
513 not use individual-level data which may raise ethic issues. Our study complies with the
514 recommendations of the GATHER statement.

515 **Background**

516 Machine learning and deep learning models have been widely applied in pandemic predictions.
517 Statistical epidemic prediction models, including SIR, SEIR, and their variants, have achieved some
518 success in infection, hospitalization, and mortality prediction tasks^{25,41,42}. To extract complex
519 temporal patterns, some works have applied the recurrent neural network (RNN) and its variants,
520 such as long short-term memory network (LSTM) and gated recurrent unit network (GRU), to
521 predict future infected and hospitalization cases²⁴⁻²⁶.

522 To further improve the spatio-temporal prediction performance, a significant line of research
523 focuses on extracting and utilizing spatial dependencies. Graph neural networks (GNN)^{4,27,43,44} and
524 metapopulation analysis models⁴⁵⁻⁴⁷ have achieved remarkable success in solving this issue. In these
525 works, counties and states are modeled as nodes in the graph, and the edges are defined using
526 geographical and sociological similarities or mobility scores. By combining the GNNs and RNNs,
527 these models can extract spatio-temporal patterns in the data and make better predictions. However,
528 most of these models rely on pre-defined location graphs. These manually defined location graphs
529 may differ greatly from the ground truth inter-regional relationships and spatial pandemic
530 transmission patterns. Besides, some metapopulation models are only applicable for infectious
531 diseases since the underlying assumption is the population flow, which makes it difficult to extract
532 other spatial patterns such as hospitalizations. Some works aim to solve this issue by adaptively
533 learning the connection weights between locations. Jin et al.⁸ and Deng et al.⁹ utilize the attention
534 mechanism to predict future infected cases in pandemics. Their work learns the connection weights
535 based on the similarities of historical case curves at different locations but largely ignores the
536 underlying social, economic, medical, and geographical similarities, which may have a profound
537 impact on the inter-location relationships. Therefore, further exploration is needed to discern how
538 best to model spatial dependencies with multi-source background data in a flexible way.

539 Another line of research focuses on integrating real-world disease transmission dynamics into
540 deep learning models. Though deep learning networks can extract complex temporal patterns, they
541 can only predict known data patterns and thus have worse long-term prediction accuracy. Integrating
542 epidemiology models such as SIR and SEIR can help deep learning models predict curves
543 resembling real-world transmission patterns. Gao et al.⁴ used an SIR model as a regularizer term in
544 the loss function to help the GAT-GRU model predict county-level COVID-19 infection case
545 numbers in the United States. Storlie et al.⁶ proposed a stochastic SIR model to predict future
546 COVID-19 cases. Though these models can be applied in the COVID-19 hospitalization prediction,

547 their main approach involves dividing the infected population into hospitalized and non-hospitalized
548 cohorts and then modifying the transmission equation accordingly. However, as mentioned in the
549 introduction, the relatively few parameters in most epidemiological models may not fully describe
550 the influences of complex underlying disease distribution, viral variants, and vaccination effects.
551 Additionally, these epidemiological models are not designed for general spatio-temporal predictions
552 and thus cannot extract and utilize inter-regional interactions. Therefore, integrating appropriate
553 real-world dynamics that can naturally model spatio-temporal hospitalizations may improve the
554 prediction performance. The Ising model is a statistical mechanics model for site spin configuration
555 estimations; it has been applied in sociology research to model social behavior by considering each
556 individual as a site⁴⁰. In this work, instead of directly using statistical methods to estimate the Ising
557 parameters in a low-dimensional and static-variable-only dataset, we combine the Ising dynamics
558 with deep learning techniques to model the spatio-temporal pandemic hospitalization patterns from
559 complex, high-dimensional multi-source data.

560 **Learning adaptative connectivity in the latent space**

561 Pandemic progression patterns have spatial similarity depending on the underlying population,
562 economic, geographic, and mobility factors in various locations. Recent works suggest that utilizing
563 these spatial similarities can guide the model to better extract progression patterns and make more
564 accurate predictions^{4,27,43,44}. In this work, instead of pre-defining a connected location graph with
565 fixed edges, we aim to learn the adaptative connectivity between locations. Concretely, we measure
566 the latent distances between locations from multiple perspectives from the static data, and then
567 normalize the distances to similarities.

568 In HOIST, each location will be embedded in a multi-dimensional latent space. The latent space
569 is created by considering the set of socio-demographic variables as dimensions so that each location
570 will have a unique position, and locations that are similar in these socio-demographic factors will
571 be embedded closely in the space (also known as the Blau space in sociology study)⁴⁸. To calculate
572 the distance of two locations in the latent space, previous works directly use the sum of Euclidean
573 distance over all dimensions⁴⁰. This is applicable in small-scale settings, but our setting is large-
574 scale and high-dimensional, containing all counties in the United States. The scale differences in
575 some factors are substantial (e.g., population size and geographic distance). Using Euclidean
576 distance may lead to biased connectivity. Furthermore, we also aim to capture the complex nonlinear
577 similarity, which is difficult for scale-invariant distance metrics such as Mahalanobis distance. In
578 this work, we calculate the distances using the graph attention mechanism⁴⁹. Concretely, for location
579 i and j , the latent distance l_{ij} is calculated as:

$$580 \quad l_{ij} = \sum_{\mathbf{K} \in \{\mathbf{M}, \mathbf{E}\}} \sigma(\mathbf{W}_{K,2}(\mathbf{W}_{K,1}\mathbf{k}_i \parallel \mathbf{W}_{K,2}\mathbf{k}_j)) + \sigma(\mathbf{W}_{D,2}(\mathbf{W}_{D,1}(d_{ij} \parallel g_{ij}))) \quad (7)$$

581 where \mathbf{k}_i denotes the i -th row vector of the \mathbf{K} matrix (i.e., the population demographics \mathbf{M} and
582 the economics and healthcare statistics \mathbf{E}), d_{ij} and g_{ij} denote the value at i -th row and j -th
583 column in the matrices \mathbf{D} and \mathbf{G} (i.e., the distance between location i and j),
584 $\mathbf{W}_{K,2}, \mathbf{W}_{K,1}, \mathbf{W}_{D,1}, \mathbf{W}_{D,2}$ are weight matrices, σ denotes the sigmoid activation function, and $(\cdot \parallel \cdot)$
585 denotes the concatenation operation. Using this attention mechanism, the model can adaptatively
586 learn the distance between two locations from multiple perspectives including demographics,
587 populations, economics, healthcare, geographic distance, and mobility. The distances are further
588 normalized to obtain the similarity s_{ij} as:

589
$$s_{ij} = \frac{\exp(l_{ij})}{\sum_k^N \exp(l_{ik})} \quad (8)$$

590 where s_{ij} indicates the normalized adaptative similarity between location i and j learned by the
 591 model. The higher the s_{ij} , the more similar the two locations. The similarity scores of all locations
 592 formulate the matrix $\mathbf{S} \in \mathbb{R}^{N \times N}$ which is used to inform how the model utilizes the learned spatial
 593 connectivity in the following sections.

594 **Modeling the external fields in Ising dynamics**

595 In the Ising model, the energy of a spin configuration \mathbf{y} of lattice sites is given by the
 596 Ising Hamiltonian I , which takes the form:

597
$$I = - \sum_i \left(e_i y_i + \sum_{\langle i,j \rangle} s_{ij} y_i y_j \right) \quad (9)$$

598 where s_{ij} denotes the interaction between two sites i and j , and e_i denotes the external field
 599 (E.F.) interacting with site i . The Ising Hamiltonian I can be considered as the sum of the energy
 600 related to the interactions between sites and the energy related to the external field. This Ising
 601 Hamiltonian form is applied to capture pandemic hospitalization patterns. First, the hospitalization
 602 patterns are highly correlated with the location-specific distributions on comorbidity, vaccination,
 603 and hospital resource usage. This can be modeled as the first term in the Ising Hamiltonian $e_i y_i$.
 604 Secondly, the hospitalization patterns are highly correlated across locations depending on the
 605 underlying socioeconomic factors. The second term in the Ising Hamiltonian matches location-
 606 correlation. We propose to use the Ising dynamics to guide the model learning process in this manner.

607 To fuse this dynamic equation into the HOIST model, the initial step is to model the external
 608 fields using Ising dynamics. More specifically, we model the external fields of a specific location
 609 from multiple perspectives. The idea is to utilize historical statistics to infer future hospitalization
 610 cases. For example, if the number of infected cases among high-risk cohorts has risen in the past
 611 few months, the number of hospitalization cases is also likely to rise soon. This temporal delay is
 612 expected since many infected patients, even those at high risk for critical illness, do not develop
 613 severe manifestations immediately. Of course, we also take vaccinations into consideration; as the
 614 number of immunized individuals increases, the hospitalization rate decreases. All sequence vectors
 615 are flattened into vectors in a historical window τ instead of just the values at timestep t (e.g.,
 616 $\mathbf{u}'_t = [\mathbf{u}_{t-\tau+1}, \mathbf{u}_{t-\tau+2}, \dots, \mathbf{u}_t]$). Likewise, we create the historical new infected case sequence \mathbf{i}'_t ,
 617 claim statistics sequence \mathbf{c}'_t , vaccination statistics \mathbf{v}'_t , and medical resource usage sequence \mathbf{u}'_t
 618 at timestep t . Note that we omit the location index i in this section because we are only discussing
 619 one specific location. The parameters of external fields are modeled as:

620
$$\mathbf{f}_I = \sigma(\phi_I(\mathbf{i}'_t)) \quad (10)$$

621
$$\mathbf{f}_C = \sigma(\phi_C(\mathbf{c}'_t)) \quad (11)$$

622
$$\mathbf{f}_V = \sigma(\phi_V(\mathbf{v}'_t)) \quad (12)$$

623
$$\mathbf{f}_U = \sigma(\phi_U(\mathbf{u}'_t)) \quad (13)$$

624 where $\phi: \mathbb{R}^F \rightarrow \mathbb{R}^F$ denotes the projection function to generate scaling factors for each
 625 sequential factor. By multiplying the scaling factors and the sequential factors, the final predictions
 626 are calculated as:

627
$$\hat{\mathbf{f}} = [\mathbf{f}_I \cdot \mathbf{i}'_t | \mathbf{f}_C \cdot \mathbf{c}'_t | -\mathbf{f}_V \cdot \mathbf{v}'_t | \mathbf{f}_U \cdot \mathbf{u}'_t] \quad (14)$$

628
$$\hat{\mathbf{h}}_t = \text{LSTM}(\hat{\mathbf{f}}, \hat{\mathbf{h}}_{t-1}) \quad (15)$$

629 Here $\text{LSTM}(\cdot)$ denotes a multi-layer perceptron to capture temporal progressions, the (\cdot)
630 operation denotes the Hadamard product and $(\cdot || \cdot)$ denotes the concatenation operation. This
631 process is essentially learning weights (i.e., \mathbf{f}_I , \mathbf{f}_C , \mathbf{f}_V and \mathbf{f}_U) for different influence factors. The
632 larger the weight, the greater the influence of the corresponding factors on the prediction result. This
633 is also why we add the negative symbol before \mathbf{f}_V , since the vaccinations should be negatively
634 correlated with hospitalization cases. By concatenating all the scaling factors, we obtain the E.F.
635 strength vector $\hat{\mathbf{f}}$. We further use an LSTM network to model the temporal progression of the E.F.

636 To generate the final predictions for location i (here we bring back the location subscript as
637 $\hat{\mathbf{h}}_{i,t}$), we calculate the weighted sum of the final hidden state from the LSTM network from other
638 locations. We use the adaptative connectivity \mathbf{S} as the connection weight as:

$$639 \quad \mathbf{z}_{i,t} = \hat{\mathbf{h}}_{i,t} + \sum_j^N s_{ij} \hat{\mathbf{h}}_{j,t} \quad (16)$$

$$640 \quad \hat{y}_{i,t} = \text{MLP}(\mathbf{z}_{i,t}) \quad (17)$$

641 In this way, the final prediction result $\hat{y}_{i,t}$ considers not only the temporal progression of the
642 pandemic and influence factors (Equation 3), but also the relevant spatial relationships (Equation 2
643 and 4).

644 **End-to-end learning with the spatio-temporal Ising loss function**

645 Our loss function consists of a prediction loss and an Ising dynamics constraint loss. First, the
646 prediction loss is calculated by using the mean square error:

$$647 \quad \mathcal{L}_p = \sum_i^N \sum_t^T (\hat{y}_{i,t} - y_{i,t})^2 \quad (18)$$

648 The second loss term is the Ising constraint loss \mathcal{L}_d , which takes the form:

$$649 \quad e_i = \sum_k^{|\hat{\mathbf{f}}_i|} \hat{f}_{i,k} \quad (19)$$

$$650 \quad \hat{y}_{i,t}^d = e_i \hat{y}_{i,t} + \sum_j^N s_{ij} \hat{y}_{i,t} \hat{y}_{j,t} \quad (20)$$

$$651 \quad \mathcal{L}_d = \sum_i^N \sum_t^T (\hat{y}_{i,t}^d - y_{i,t})^2 \quad (21)$$

652 The term e_i denotes the summation over all dimensions of $\hat{\mathbf{f}}_i$, and $\hat{f}_{i,k}$ denotes the k -th
653 dimension in the $\hat{\mathbf{f}}_i$ vector, which turns the E.F. vector into a scalar, denoting the E.F. strength. s_{ij}
654 is the value at the i -th row, j -th column in the \mathbf{S} matrix, which is the similarity score between
655 location i and j . \mathcal{L}_d is essentially another mean square error loss between the ground truth value
656 and the estimated value using the Ising dynamics (i.e., $\hat{y}_{i,t}^d$). In the original Ising dynamics setting,
657 the system's energy should be as low as possible to keep the system stable. Here, we use the same
658 idea to reduce the prediction error \mathcal{L}_d as part of our loss function. It is worth noting that $\hat{y}_{i,t}$ is the
659 final prediction result and $\hat{y}_{i,t}^d$ is only used as an auxiliary output to optimize the Ising constraint
660 parameters. The final loss takes the form:

$$661 \quad \mathcal{L} = \mathcal{L}_d + \mathcal{L}_p \quad (22)$$

662 By optimizing the Ising constraint loss and the prediction loss together, the model can extract
663 the temporal hospitalization progression patterns as well as optimize the spatial adaptative
664 connectivity. Using the Ising dynamics as a constraint instead of directly using \hat{y}^d as the prediction
665 result and only optimizing \mathcal{L}_d allows the model to have more flexibility to learn spatio-temporal
666 patterns from high-dimensional data.

667 **Data Availability**

668 The mobility scores are collected from the Multiscale Dynamic Human Mobility Flow
669 Dataset¹¹ (<https://github.com/GeoDS/COVID19USFlows>). The census features are collected from
670 the county-level census dataset provided by the US County-level Dataset¹²
671 (https://github.com/JieYingWu/COVID-19_US_County-level_Summaries). The daily new cases
672 are collected from the Johns Hopkins COVID-19 Data Repository¹³
673 (<https://github.com/CSSEGISandData/COVID-19>). The medical resource usage statistics are
674 collected from HealthData.gov¹⁷ ([https://healthdata.gov/Hospital/COVID-19-Reported-Patient-](https://healthdata.gov/Hospital/COVID-19-Reported-Patient-Impact-and-Hospital-Capa/anag-cw7u)
675 [Impact-and-Hospital-Capa/anag-cw7u](https://healthdata.gov/Hospital/COVID-19-Reported-Patient-Impact-and-Hospital-Capa/anag-cw7u)). All the processed public data are available at
676 <https://github.com/v1xerunt/HOIST>. The claims data contains sensitive healthcare information and
677 are extracted from <https://www.iqvia.com/solutions/real-world-evidence/>, which can be accessed on
678 request. Our model can be trained without using claims data. Source data of tables and figures are
679 provided with this paper.

680 **Code Availability**

681 The codes for model construction, training and inference used in this paper are publicly
682 available at <https://github.com/v1xerunt/HOIST>. The visualization results are available at
683 <https://v1xerunt.github.io/HOIST/>.

684 **References**

- 685 1. Centers for Disease Control and Prevention. CDC COVID Data Tracker. Accessed May 01,
686 2022. <https://covid.cdc.gov/covid-data-tracker/#datatracker-home>.
- 687 2. Hassan, E.M. & Mahmoud, H.N. Impact of multiple waves of COVID-19 on healthcare
688 networks in the United States. *PloS one* **16**, e0247463 (2021).
- 689 3. Centers for Disease Control and Prevention. Disparities in COVID-19 Vaccination Coverage
690 Between Urban and Rural Counties. Accessed May 2022.
691 <https://www.cdc.gov/mmwr/volumes/71/wr/mm7109a2.htm>.
- 692 4. Gao, J., Sharma, R., Qian, C., *et al.* STAN: spatio-temporal attention network for pandemic
693 prediction using real-world evidence. *Journal of the American Medical Informatics Association*
694 **28**, 733-743 (2021).
- 695 5. Kargas, N., Qian, C., Sidiropoulos, N.D., *et al.* Stelar: Spatio-temporal tensor factorization with
696 latent epidemiological regularization. in *the 2021 AAAI Conference on Artificial Intelligence*,
697 Vol. 35 4830-4837 (2021).
- 698 6. Storlie, C.B., Rojas, R.L., Demuth, G.O., *et al.* A Hierarchical Bayesian Model for Stochastic
699 Spatiotemporal SIR Modeling and Prediction of COVID-19 Cases and Hospitalizations. *arXiv*
700 *preprint arXiv:2104.04033* (2021).
- 701 7. Fan, C., Meng, Y., Sun, X., *et al.* Parameter Estimation for the SEIR Model Using Recurrent
702 Nets. *arXiv preprint arXiv:2105.14524* (2021).

- 703 8. Jin, X., Wang, Y.-X. & Yan, X. Inter-series attention model for covid-19 forecasting. in *the 2021*
704 *SIAM International Conference on Data Mining (SDM)* 495-503 (SIAM, 2021).
- 705 9. Deng, S., Wang, S., Rangwala, H., Wang, L. & Ning, Y. Cola-GNN: Cross-location attention
706 based graph neural networks for long-term ILI prediction. in *the 29th ACM International*
707 *Conference on Information & Knowledge Management* 245-254 (2020).
- 708 10. Cipra, B.A. An introduction to the Ising model. *The American Mathematical Monthly* **94**, 937-
709 959 (1987).
- 710 11. Kang, Y., Gao, S., Liang, Y., *et al.* Multiscale dynamic human mobility flow dataset in the US
711 during the COVID-19 epidemic. *Scientific data* **7**, 1-13 (2020).
- 712 12. Killeen, B.D., Wu, J.Y., Shah, K., *et al.* A county-level dataset for informing the United States'
713 response to COVID-19. *arXiv preprint arXiv:2004.00756* (2020).
- 714 13. Dong, E., Du, H. & Gardner, L. An interactive web-based dashboard to track COVID-19 in real
715 time. *The Lancet infectious diseases* **20**, 533-534 (2020).
- 716 14. Centers for Disease Control and Prevention. People with Certain Medical Conditions. Accessed
717 Aug 1, 2022. [https://www.cdc.gov/coronavirus/2019-ncov/need-extra-precautions/people-](https://www.cdc.gov/coronavirus/2019-ncov/need-extra-precautions/people-with-medical-conditions.html)
718 [with-medical-conditions.html](https://www.cdc.gov/coronavirus/2019-ncov/need-extra-precautions/people-with-medical-conditions.html).
- 719 15. Sundararajan, V., Henderson, T., Perry, C., *et al.* New ICD-10 version of the Charlson
720 comorbidity index predicted in-hospital mortality. *Journal of clinical epidemiology* **57**, 1288-
721 1294 (2004).
- 722 16. IQVIA. Harness the power of Real World Data. Accessed Aug 1, 2022.
723 <https://www.iqvia.com/solutions/real-world-evidence/real-world-data-and-insights>.
- 724 17. HealthData. COVID-19 Reported Patient Impact and Hospital Capacity by State. Accessed Aug
725 1, 2022. [https://healthdata.gov/dataset/COVID-19-Reported-Patient-Impact-and-Hospital-](https://healthdata.gov/dataset/COVID-19-Reported-Patient-Impact-and-Hospital-Capa/6xf2-c3ie/data)
726 [Capa/6xf2-c3ie/data](https://healthdata.gov/dataset/COVID-19-Reported-Patient-Impact-and-Hospital-Capa/6xf2-c3ie/data).
- 727 18. Gao, J., Yang, C., Heintz, J., *et al.* MedML: Fusing medical knowledge and machine learning
728 models for early pediatric COVID-19 hospitalization and severity prediction. *Iscience* **25**,
729 104970 (2022).
- 730 19. The BARDA Community Challenge. BARDA Community Challenge - Pediatric COVID-19
731 Data Challenge. Accessed May 04, 2022.
732 <https://www.synapse.org/#!/Synapse:syn25875374/wiki/>.
- 733 20. Lin, Z., Trivedi, S. & Sun, J. Conformal Prediction Intervals with Temporal Dependence. *arXiv*
734 *preprint arXiv:2205.12940* (2022).
- 735 21. Paszke, A., Gross, S., Massa, F., *et al.* Pytorch: An imperative style, high-performance deep
736 learning library. in *Advances in neural information processing systems*, Vol. 32 (2019).
- 737 22. Li, M.L., Bouardi, H.T., Lami, O.S., *et al.* Forecasting COVID-19 and analyzing the effect of
738 government interventions. *Operations Research* (2022).
- 739 23. Byrd, R.H., Gilbert, J.C. & Nocedal, J. A trust region method based on interior point techniques
740 for nonlinear programming. *Mathematical programming* **89**, 149-185 (2000).
- 741 24. Kavouras, I., Kaselimi, M., Protopapadakis, E., *et al.* COVID-19 Spatio-Temporal Evolution
742 Using Deep Learning at a European Level. *Sensors* **22**, 3658 (2022).
- 743 25. Yang, Z., Zeng, Z., Wang, K., *et al.* Modified SEIR and AI prediction of the epidemics trend of
744 COVID-19 in China under public health interventions. *Journal of thoracic disease* **12**, 165
745 (2020).
- 746 26. Nikparvar, B., Rahman, M., Hatami, F. & Thill, J.-C. Spatio-temporal prediction of the COVID-

- 747 19 pandemic in US counties: modeling with a deep LSTM neural network. *Scientific reports* **11**,
748 1-12 (2021).
- 749 27. Kapoor, A., Ben, X., Liu, L., *et al.* Examining covid-19 forecasting using spatio-temporal graph
750 neural networks. *arXiv preprint arXiv:2007.03113* (2020).
- 751 28. Callaway, E. Fast-spreading COVID variant can elude immune responses. *Nature* **589**, 500-502
752 (2021).
- 753 29. Eyre, D.W., Taylor, D., Purver, M., *et al.* Effect of Covid-19 vaccination on transmission of
754 alpha and delta variants. *New England Journal of Medicine* **386**, 744-756 (2022).
- 755 30. Kuswardhani, R.T., Henrina, J., Pranata, R., *et al.* Charlson comorbidity index and a composite
756 of poor outcomes in COVID-19 patients: A systematic review and meta-analysis. *Diabetes &*
757 *Metabolic Syndrome: Clinical Research & Reviews* **14**, 2103-2109 (2020).
- 758 31. Christensen, D.M., Strange, J.E., Gislason, G., *et al.* Charlson comorbidity index score and risk
759 of severe outcome and death in Danish COVID-19 patients. *Journal of general internal*
760 *medicine* **35**, 2801-2803 (2020).
- 761 32. Tenforde, M.W., Self, W.H., Adams, K., *et al.* Association between mRNA vaccination and
762 COVID-19 hospitalization and disease severity. *Jama* **326**, 2043-2054 (2021).
- 763 33. Centers for Disease Control and Prevention. Risk for COVID-19 Infection, Hospitalization, and
764 Death By Age Group. Accessed Dec 2022. [https://www.cdc.gov/coronavirus/2019-ncov/covid-](https://www.cdc.gov/coronavirus/2019-ncov/covid-data/investigations-discovery/hospitalization-death-by-age.html)
765 [data/investigations-discovery/hospitalization-death-by-age.html](https://www.cdc.gov/coronavirus/2019-ncov/covid-data/investigations-discovery/hospitalization-death-by-age.html).
- 766 34. Centers for Disease Control and Prevention. Risk for COVID-19 Infection, Hospitalization, and
767 Death By Race/Ethnicity. Accessed Dec 2022. [https://www.cdc.gov/coronavirus/2019-](https://www.cdc.gov/coronavirus/2019-ncov/covid-data/investigations-discovery/hospitalization-death-by-race-ethnicity.html)
768 [ncov/covid-data/investigations-discovery/hospitalization-death-by-race-ethnicity.html](https://www.cdc.gov/coronavirus/2019-ncov/covid-data/investigations-discovery/hospitalization-death-by-race-ethnicity.html).
- 769 35. Services, C.f.M.M. Medicare COVID-19 Vaccine Shot Payment. Accessed Dec 2022.
770 <https://www.cms.gov/medicare/covid-19/medicare-covid-19-vaccine-shot-payment>.
- 771 36. FAIRHealth. COVID-19 Cost Tracker. Accessed Dec 2022. [https://www.fairhealth.org/states-](https://www.fairhealth.org/states-by-the-numbers/covid19-heatmap)
772 [by-the-numbers/covid19-heatmap](https://www.fairhealth.org/states-by-the-numbers/covid19-heatmap).
- 773 37. The New York Times. COVID-19 Vaccinations: County and State Tracker. Accessed Dec 2022.
774 <https://www.nytimes.com/interactive/2020/us/covid-19-vaccine-doses.html>.
- 775 38. Gao, J., Yang, C., Heintz, G., *et al.* MedML: Fusing Medical Knowledge and Machine Learning
776 Models for Early Pediatric COVID-19 Hospitalization and Severity Prediction. *arXiv preprint*
777 *arXiv:2207.12283* (2022).
- 778 39. Bennett, T.D., Moffitt, R.A., Hajagos, J.G., *et al.* Clinical characterization and prediction of
779 clinical severity of SARS-CoV-2 infection among US adults using data from the US National
780 COVID Cohort Collaborative. *JAMA network open* **4**, e2116901-e2116901 (2021).
- 781 40. Godoy-Lorite, A. & Jones, N.S. Inference and influence of network structure using snapshot
782 social behavior without network data. *Science Advances* **7**, eabb8762 (2021).
- 783 41. Pei, S. & Shaman, J. Initial simulation of SARS-CoV2 spread and intervention effects in the
784 continental US. *MedRxiv* (2020).
- 785 42. Albani, V.V., Velho, R.M. & Zubelli, J.P. Estimating, monitoring, and forecasting COVID-19
786 epidemics: a spatiotemporal approach applied to NYC data. *Scientific Reports* **11**, 1-15 (2021).
- 787 43. Panagopoulos, G., Nikolentzos, G. & Vazirgiannis, M. Transfer graph neural networks for
788 pandemic forecasting. in *Proceedings of the AAAI Conference on Artificial Intelligence*, Vol. 35
789 4838-4845 (2021).
- 790 44. Skianis, K., Nikolentzos, G., Gallix, B., Thiebaut, R. & Exarchakis, G. Predicting COVID-19

791 positivity and hospitalization with multi-scale graph neural networks. *Preprint* (2022).

792 45. Colizza, V. & Vespignani, A. Epidemic modeling in metapopulation systems with heterogeneous
793 coupling pattern: Theory and simulations. *Journal of theoretical biology* **251**, 450-467 (2008).

794 46. Calvetti, D., Hoover, A.P., Rose, J. & Somersalo, E. Metapopulation network models for
795 understanding, predicting, and managing the coronavirus disease COVID-19. *Frontiers in*
796 *Physics* **8**, 261 (2020).

797 47. Coletti, P., Libin, P., Petrof, O., *et al.* A data-driven metapopulation model for the Belgian
798 COVID-19 epidemic: assessing the impact of lockdown and exit strategies. *BMC infectious*
799 *diseases* **21**, 1-12 (2021).

800 48. McPherson, M. A Blau space primer: prolegomenon to an ecology of affiliation. *Industrial and*
801 *Corporate Change* **13**, 263-280 (2004).

802 49. Veličković, P., Cucurull, G., Casanova, A., *et al.* Graph attention networks. *arXiv preprint*
803 *arXiv:1710.10903* (2017).

804 Acknowledgements

805 This work was supported by NSF award SCH-2205289, SCH-2014438, IIS-2034479, NIH
806 award R01 1R01NS107291-01, IQVIA, and OSF Healthcare. Junyi Gao acknowledges the receipt
807 of studentship awards from the Health Data Research UK-The Alan Turing Institute Wellcome PhD
808 Programme in Health Data Science (Grant Ref: 218529/Z/19/Z). We thank Zhen Lin from
809 University of Illinois Urbana Champaign for assisting with the model uncertainty estimation. Icons
810 in the figures are designed using resources from Flaticon.com. For the purpose of open access, the
811 author has applied a Creative Commons Attribution (CC BY) licence to any Author Accepted
812 Manuscript version arising from this submission.

813 Author Contributions Statement

814 Junyi Gao processed the feature and built the model. George Heintz, Dr. Jimeng Sun, and Dr.
815 Adam Cross provided technical and clinical guidance. All authors participated in report writing. All
816 authors declare that they have no conflicts of interest.

817 Competing Interests Statement

818 We declare that none of the authors have competing financial or non-financial interests.

819 Tables

820 **Table 1** Performance of 28-day hospitalization prediction. The performance numbers are mean (std). The
821 bold values denote the best results. The asterisk * denotes the performance differences between HOIST
822 and the best baseline models (ACTS) are significant based on the two-sided t-test results ($p < 0.001$).
823 Source data are provided as a Source Data file.

Model	MSE ($\times 10^5$)	MAE	R ²	CCC
DELPHI-SEIR	400.3 (-)	1,647 (-)	<-1	0.02 (-)
GRU	149.2 (6.6)	897.7 (20.9)	-0.04 (0.04)	0.27 (0.20)
LSTM	133.9 (6.9)	826.6 (30.0)	0.06 (0.04)	0.48 (0.10)
ColaGNN	138.5 (9.5)	801.9 (32.1)	0.10 (0.13)	0.52 (0.09)
ACTS	127.9 (14.1)	732.1 (45.3)	0.19 (0.15)	0.60 (0.10)
CovidGNN	181.0 (46.2)	1,048.0 (126.2)	-0.26 (0.18)	0.18 (0.16)

STAN	148.3 (30.7)	948.2 (68.4)	-0.06 (0.46)	0.18 (0.12)
HOIST-Risk	65.2 (14.7)	530.6 (59.5)	0.41 (0.21)	0.71 (0.08)
HOIST-Vaccination	62.1 (13.2)	515.3 (42.3)	0.45 (0.24)	0.78 (0.07)
HOIST-AC	73.4 (38.4)	562.5 (87.9)	0.27 (0.30)	0.68 (0.15)
HOIST-Ising	135.0 (15.4)	735.5 (28.6)	0.17 (0.14)	0.39 (0.07)
HOIST	38.5 (10.2)*	368.7 (18.7)*	0.60 (0.16)*	0.89 (0.02)*
p-value	3e-6	2e-7	1e-5	7e-4

824

825

826 **Table 2** NNT for hospitalization and death of the top 15 locations ranked by the cost ratio. Source data
827 are provided as a Source Data file.

County	State	Hospitalization NNT	Adjusted NNT	Cost ratio
Butte	Idaho	130	73	60.3
Woodbury	Iowa	76	44	34.5
Toole	Montana	230	130	34.5
Sheridan	Montana	204	115	34.0
Broadwater	Montana	186	109	33.7
Mineral	Nevada	273	159	32.1
Garfield	Washington	156	89	31.8
Stonewall	Texas	71	42	31.8
Lincoln	Nevada	201	114	31.2
Stanton	Kansas	101	67	29.2
Oneida	Idaho	287	163	28.7
Bowman	North Dakota	142	81	28.1
Phillips	Montana	234	132	27.4
Ness	Kansas	145	84	25.2
Teton	Montana	308	172	25.0

828

829 Figure Captions

830 **Figure 1** The proposed HOIST model.

831 We use static data to calculate the latent distances between locations. The latent distances are then used
832 to calculate the adaptative connectivity of the location graph. The dynamic data are used to estimate the
833 External Fields (E.F.s) and then generate predictions using the LSTM network. We use the Ising
834 dynamics to regularize the spatio-temporal prediction results using the estimated E.F.s and the
835 adaptative connectivity.

836

837 **Figure 2** Prediction performance plots under different lengths of prediction window L .

838 Data are presented as mean values +/- standard deviations. The error bars are standard deviations over
839 5 experiments with random initializations with $n=2,299$ locations. Source data are provided as a Source
840 Data file.

841

842 **Figure 3** Prediction performance under different time split in MSE (A), MAE (B) and CCC (C).

843 Each dot denotes a testing phase. Source data are provided as a Source Data file.

844

845 **Figure 4** Temporal change of external field weights for vaccination features.

846 Source data are provided as a Source Data file.

847

848 **Figure 5** Predicted hospitalization hotspot and error map by HOIST.

849 **a.** Predicted hospitalization hotspot map in future 28 days by HOIST, colored by case count. West coast,

850 Northeast coast and Midwest areas generally have high hospitalization case counts. **b.** Predicted

851 hospitalization hotspot map in future 28 days by HOIST, colored by hospitalization ratio. We find two

852 example locations San Diego county (A) and Riverside county (B) along the West coast – have very high

853 case counts but only medium-level hospitalization ratios. **c.** Prediction errors for locations with more

854 than 100 cases in the testing time window, colored by mean average percentage error. HOIST achieves

855 low prediction errors on most locations. Source data are provided as a Source Data file.

856

857 **Figure 6** Predicted hospitalization and infected case count curves for Effingham, Georgia.

858 **a.** Predicted curve by HOIST. The line denotes the mean value and the shadowed area denotes the

859 prediction interval with 90% confidence. **b.** Curve of infected case count. Source data are provided as a

860 Source Data file.

861

862 **Figure 7** County-level NNT and cost ratio heatmap.

863 **a.** Predicted NNT heatmap by HOIST, colored by NNT_h . Red locations indicate that only few vaccine

864 shots can help reduce a hospitalization case. **b.** Race-adjusted NNT heatmap by HOIST, colored by

865 NNT_a . The spatial pattern is similar to the unadjusted map but some locations are affected by the race

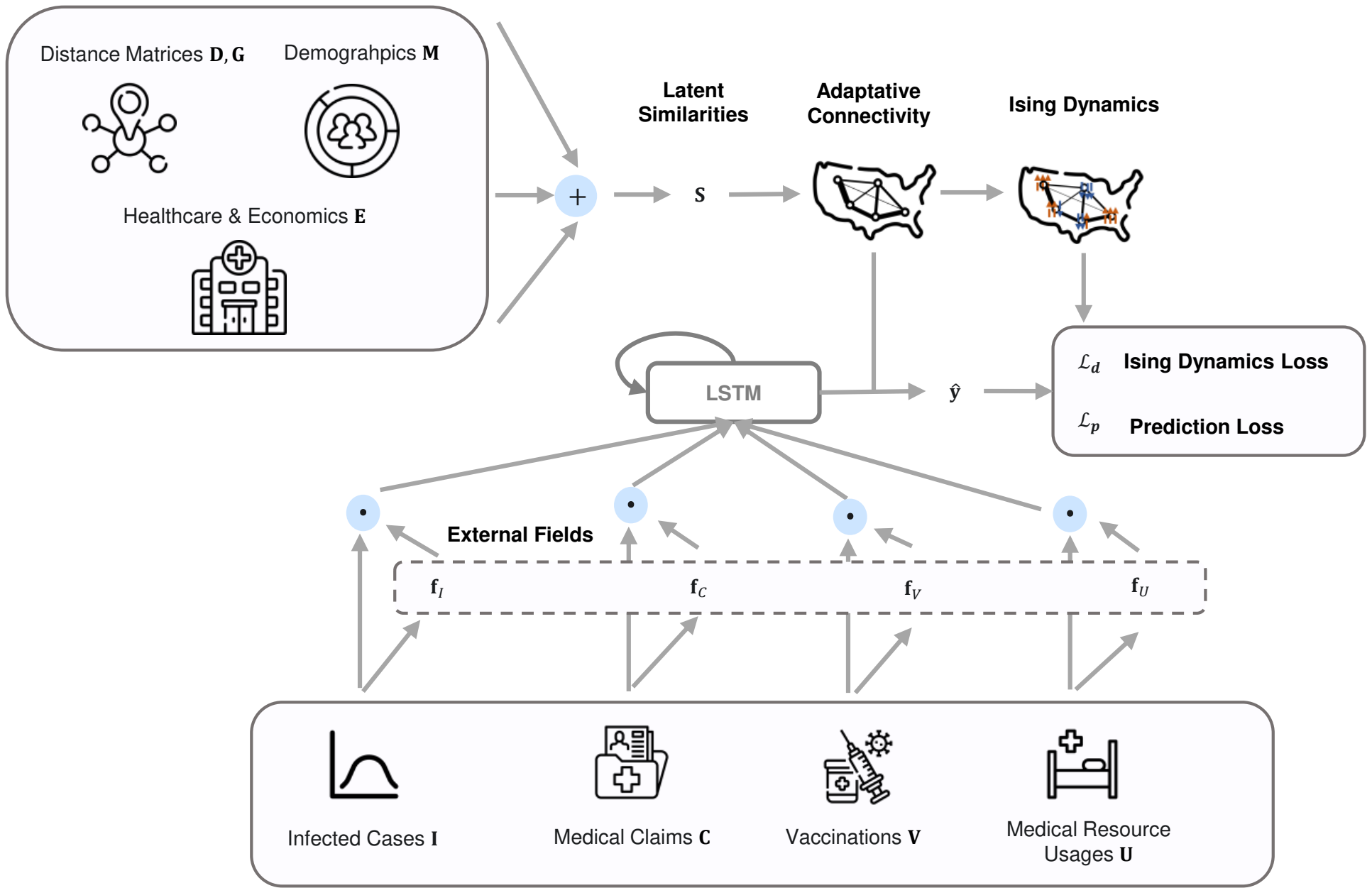
866 percentage. **c.** Heatmap of cost ratio between hospitalization costs and vaccination costs. Red locations

867 indicate that they can save healthcare costs by giving more vaccinations (i.e., cost ratio > 1). Source data

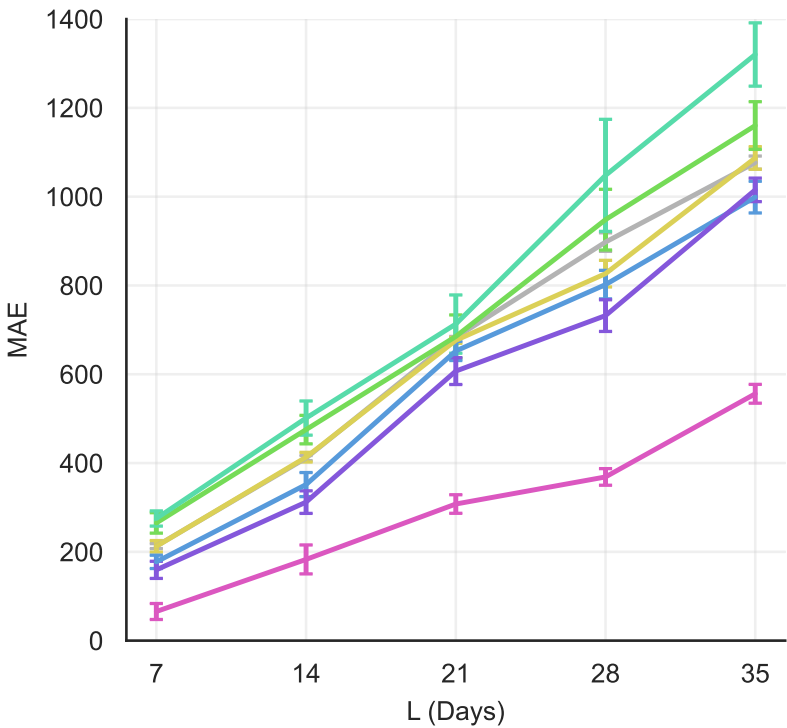
868 are provided as a Source Data file.

869

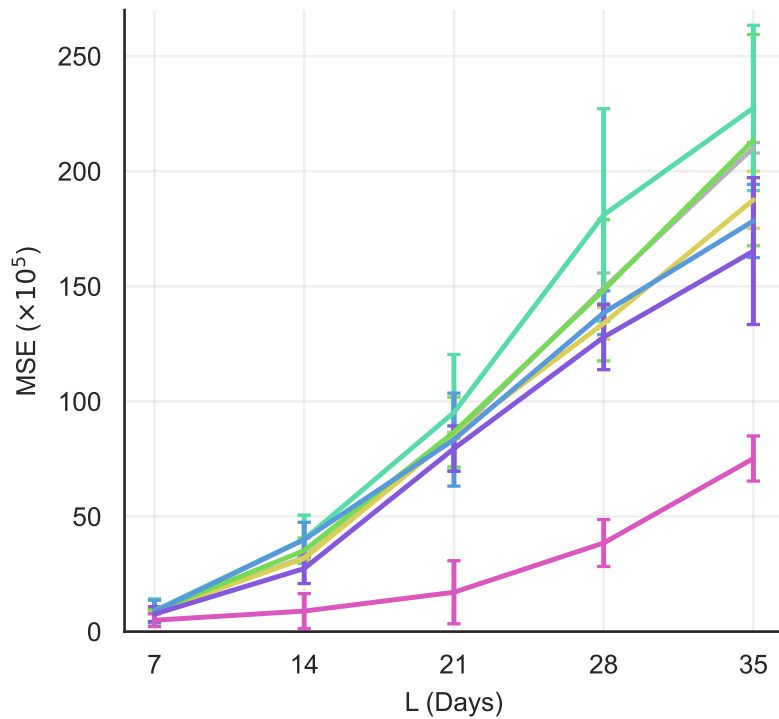
Static Data



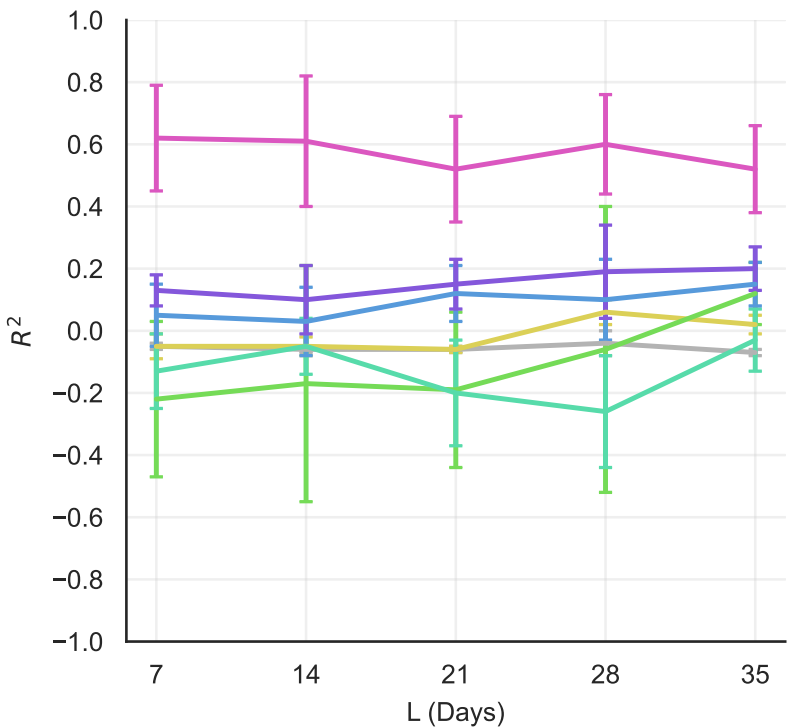
Dynamic Data



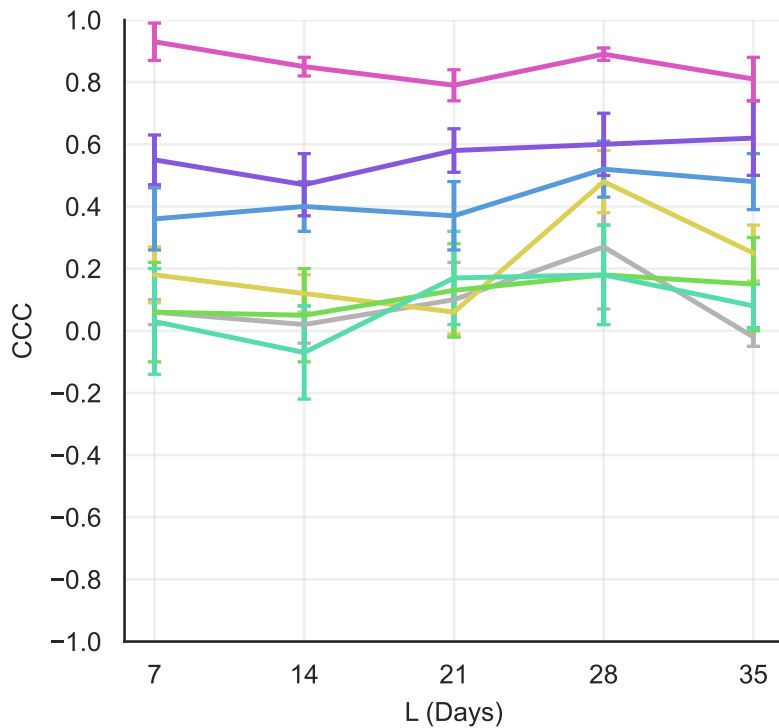
(a). MAE



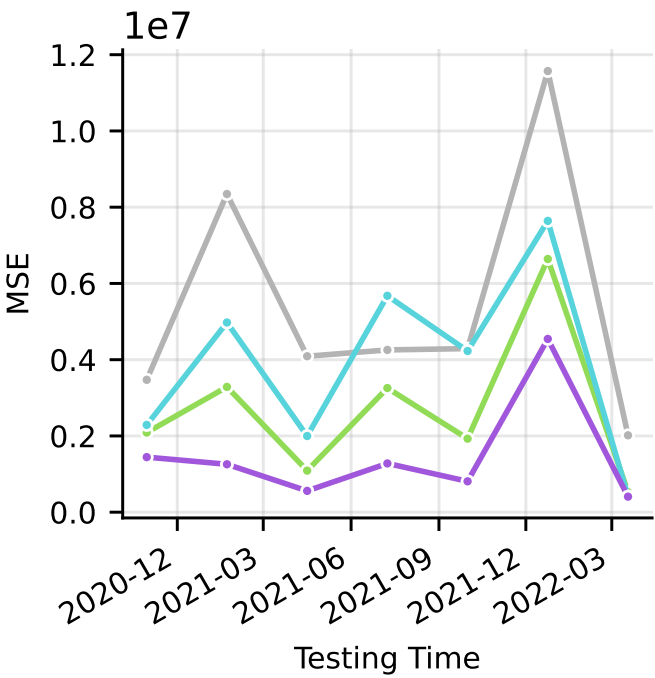
(b). MSE



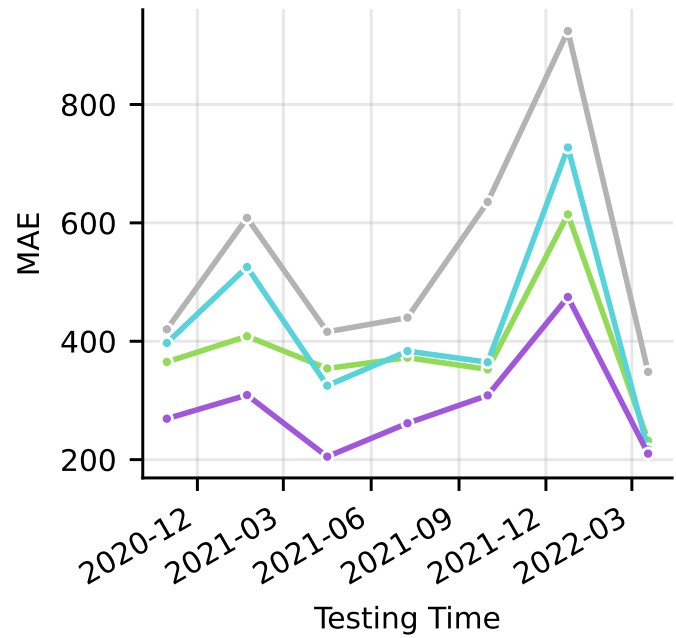
(c). R^2



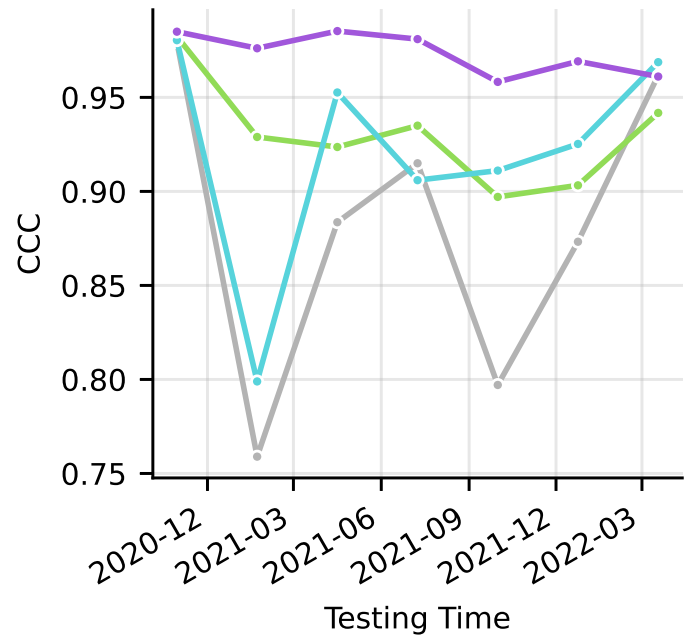
(d). CCC



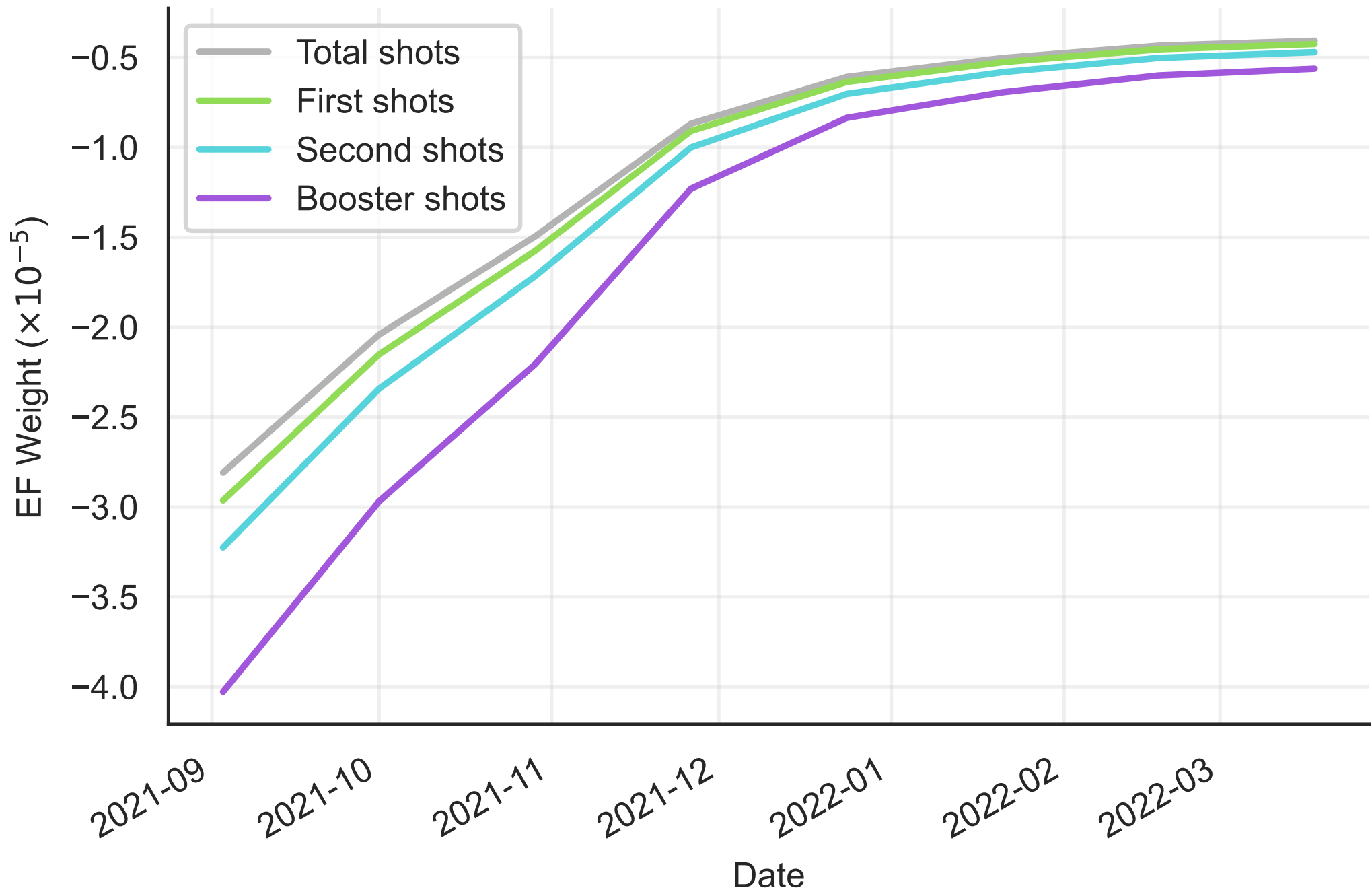
(A). MSE

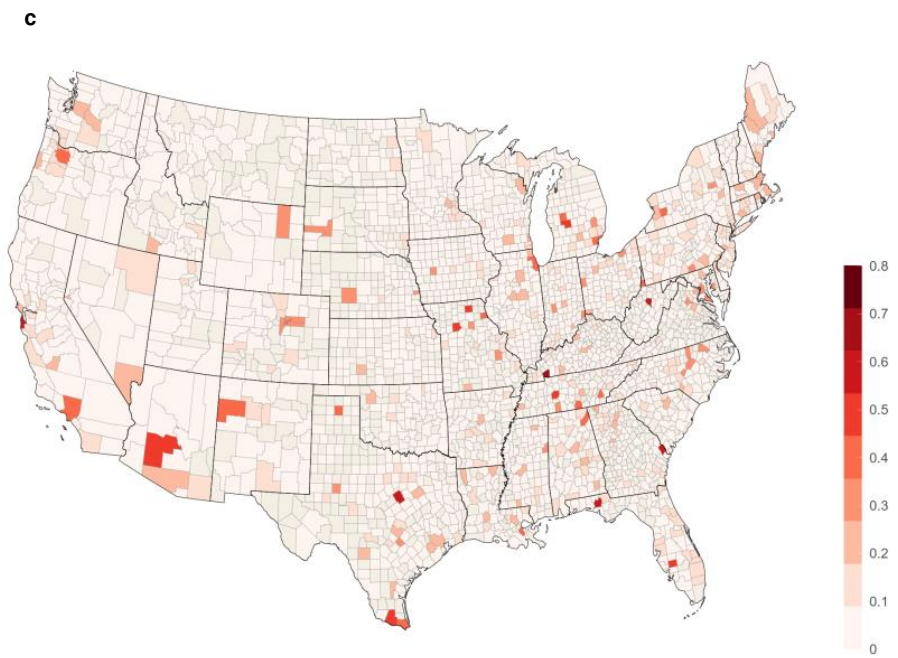
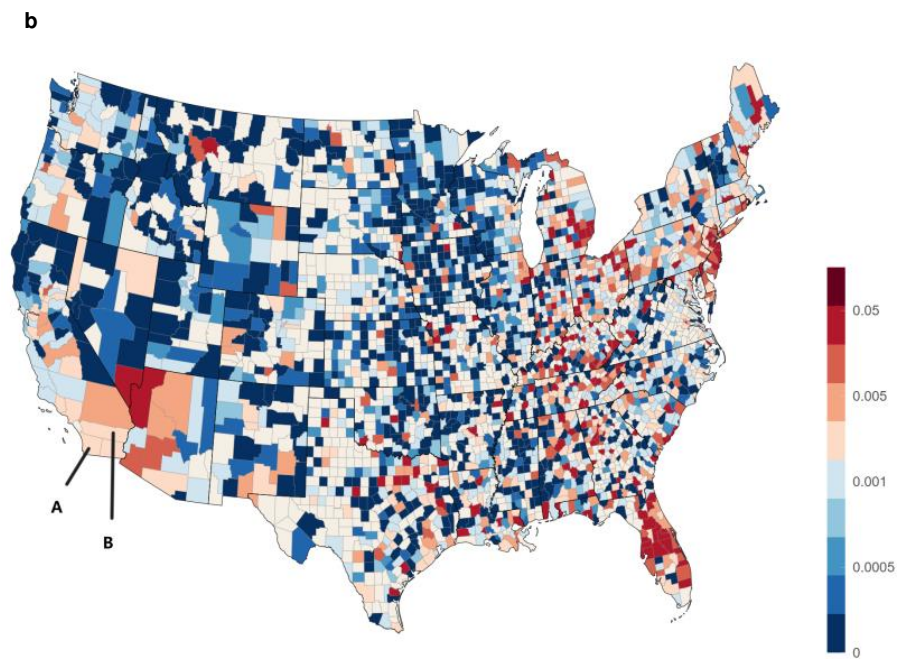
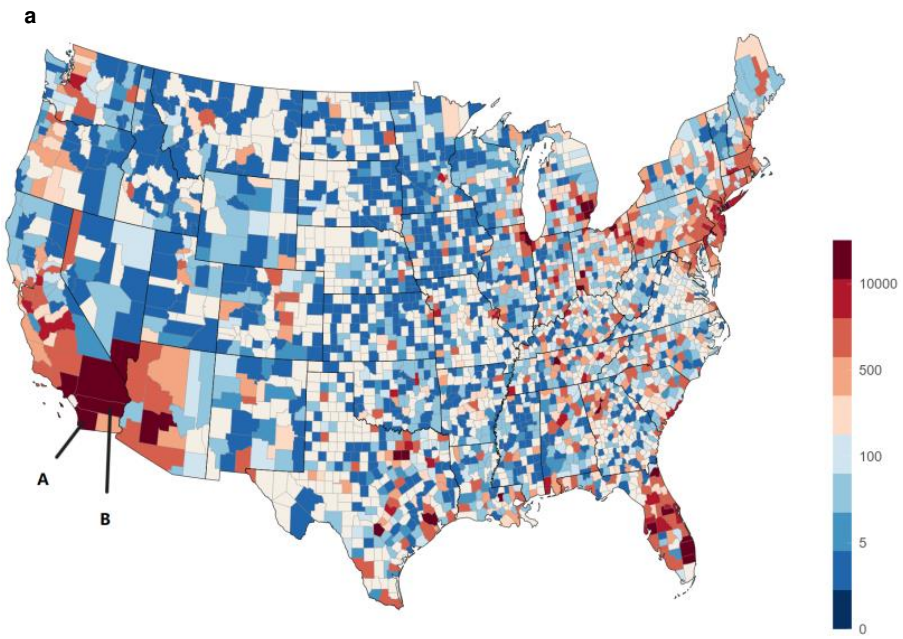


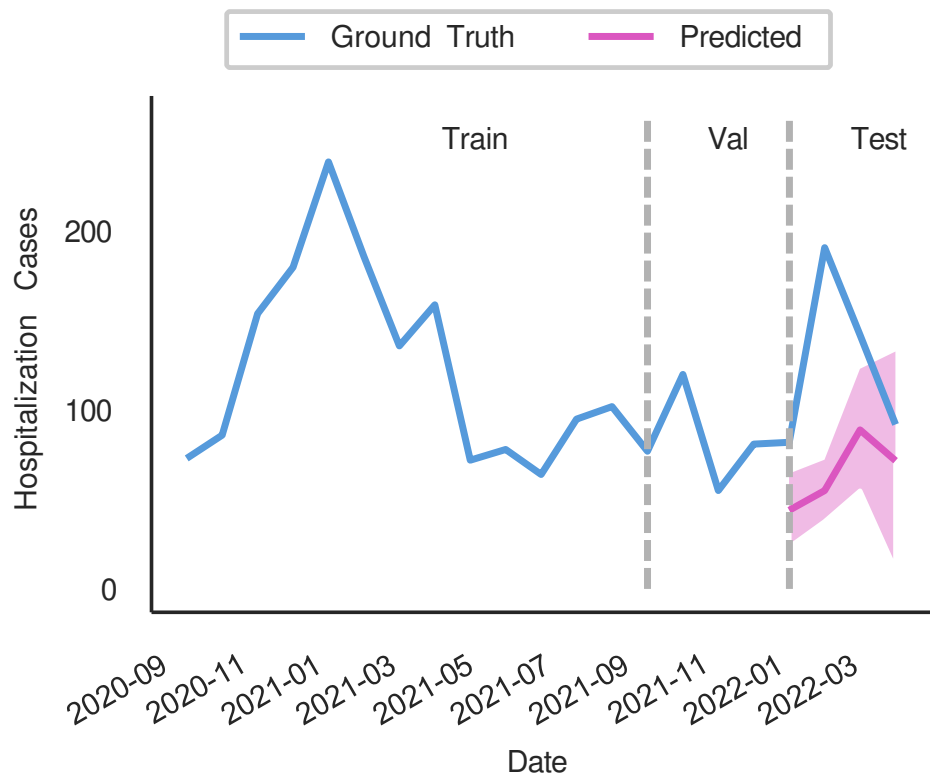
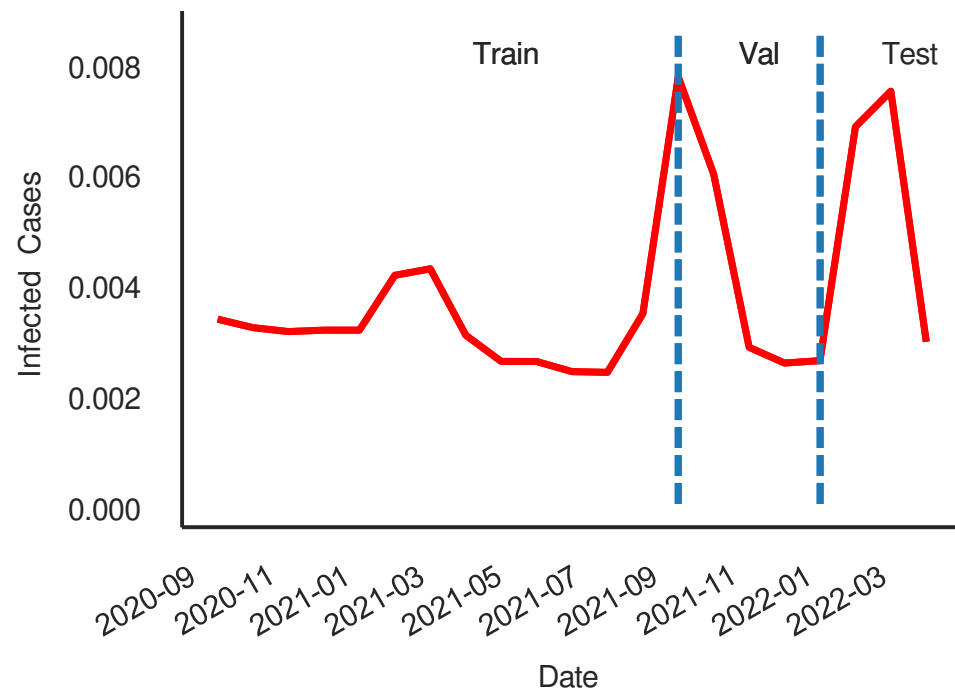
(B). MAE



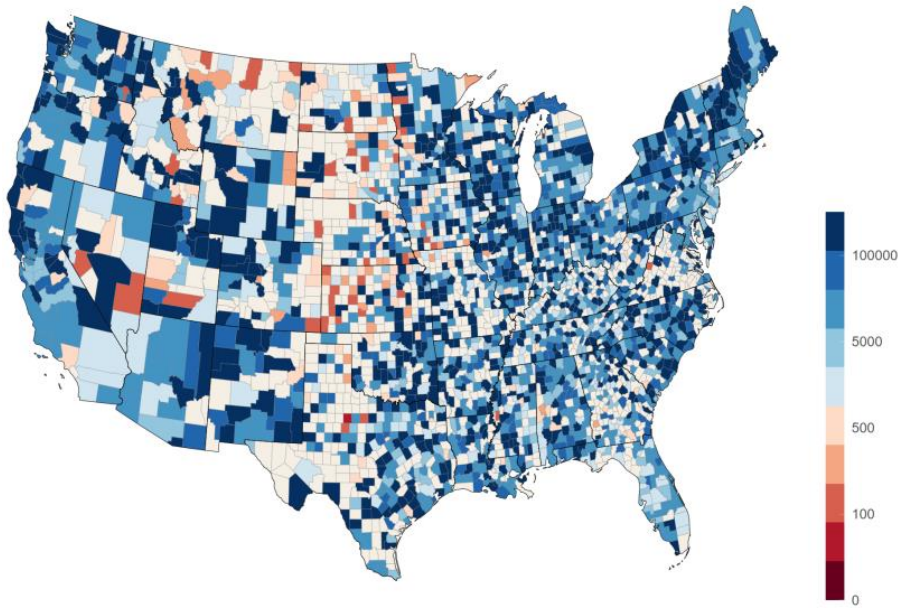
(C). CCC



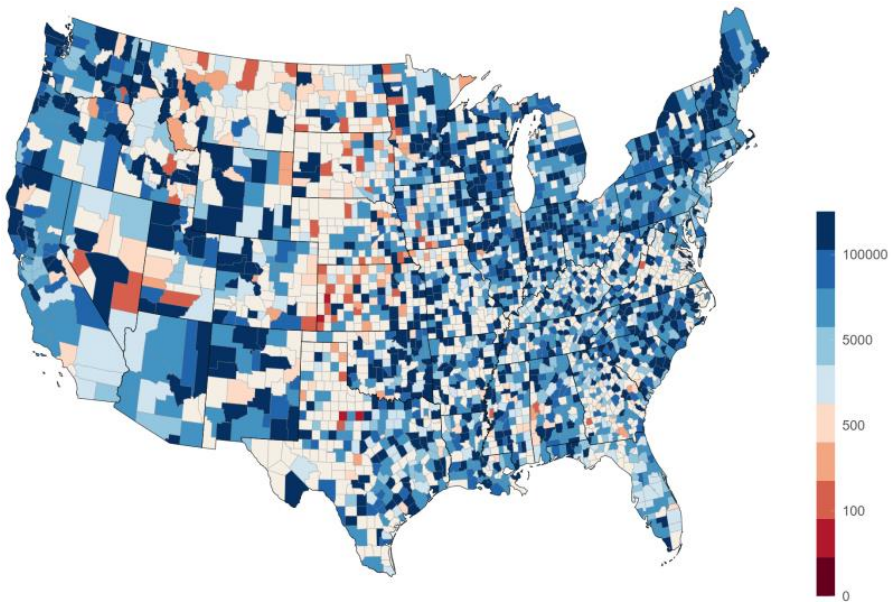


a**b**

a



b



c

